

This discussion paper is/has been under review for the journal Geoscientific Model Development (GMD). Please refer to the corresponding final paper in GMD if available.

Evaluation of a near-global eddy-resolving ocean model

P. R. Oke, D. A. Griffin, A. Schiller, R. J. Matear, R. Fiedler, J. Mansbridge, A. Lenton, M. Cahill, M. A. Chamberlain, and K. Ridgway

Centre for Australian Weather and Climate Research, CSIRO Marine and Atmospheric Research, GPO Box 1538, Hobart TAS 7001, Australia

Received: 26 November 2012 – Accepted: 27 November 2012
– Published: 18 December 2012

Correspondence to: P. R. Oke (peter.oke@csiro.au)

Published by Copernicus Publications on behalf of the European Geosciences Union.

GMDD

5, 4305–4354, 2012

Evaluation of a near-global eddy-resolving ocean model

P. R. Oke et al.

[Title Page](#)

[Abstract](#)

[Introduction](#)

[Conclusions](#)

[References](#)

[Tables](#)

[Figures](#)



[Back](#)

[Close](#)

[Full Screen / Esc](#)

[Printer-friendly Version](#)

[Interactive Discussion](#)



Abstract

Analysis of the variability in an 18-yr run of a near-global, eddy-resolving ocean general circulation model coupled with biogeochemistry is presented. Comparisons between modelled and observed mean sea level (MSL), mixed-layer depth (MLD), sea-level anomaly (SLA), sea-surface temperature (SST), and Chlorophyll *a* indicate that the model variability is realistic. We find some systematic errors in the modelled MLD, with the model generally deeper than observations, that results in errors in the Chlorophyll *a*, owing to the strong biophysical coupling. We evaluate several other metrics in the model, including the zonally-averaged seasonal cycle of SST, meridional overturning, volume transports through key Straits and passages, zonal averaged temperature and salinity, and El Nino-related SST indices. We find that the modelled seasonal cycle in SST is 0.5–1.5 °C weaker than observed; volume transports of the Antarctic Circumpolar Current, the East Australian Current, and Indonesian Throughflow are in good agreement with observational estimates; and the correlation between the modelled and observed NINO SST indices exceed 0.91. Most aspects of the model circulation are realistic. We conclude that the model output is suitable for broader analysis to better understand ocean dynamics and ocean variability.

1 Introduction

The purpose of this paper is to describe and assess a new near-global eddy-resolving ocean model, developed under Bluelink – a partnership between CSIRO, the Bureau of Meteorology, and the Royal Australian Navy. The goal of the Bluelink project is to develop capabilities in ocean forecasting and hindcasting. Bluelink is Australia's main contribution to the Global Ocean Data Assimilation Experiment (GODAE; Smith, 2000), and its successor GODAE OceanView (www.godae-oceanview.org). The Bluelink ocean model, called the Ocean Forecasting Australia Model (OFAM), has been developed over many years. The first and second versions of OFAM (OFAM1 and OFAM2)

GMDD

5, 4305–4354, 2012

Evaluation of a near-global eddy-resolving ocean model

P. R. Oke et al.

[Title Page](#)

[Abstract](#)

[Introduction](#)

[Conclusions](#)

[References](#)

[Tables](#)

[Figures](#)

[⏪](#)

[⏩](#)

[◀](#)

[▶](#)

[Back](#)

[Close](#)

[Full Screen / Esc](#)

[Printer-friendly Version](#)

[Interactive Discussion](#)



Evaluation of a near-global eddy-resolving ocean model

P. R. Oke et al.

[Title Page](#)

[Abstract](#)

[Introduction](#)

[Conclusions](#)

[References](#)

[Tables](#)

[Figures](#)



[Back](#)

[Close](#)

[Full Screen / Esc](#)

[Printer-friendly Version](#)

[Interactive Discussion](#)

were eddy-resolving in the 90°-sector centred on Australia and south of about 20° N. The latest version of OFAM (OFAM3) is a major improvement over previous versions, with the eddy-resolving region being extended to all longitudes and between 75° S–75° N, the addition of biogeochemistry and improvements to model parameterisations and forcing.

A brief history of the development of OFAM follows. Results from OFAM1 were first described by Oke et al. (2005), demonstrating that when constrained by data assimilation, OFAM produces reanalysed fields that were mostly in good agreement with with-held observations. Oke and Schiller (2007) described a series of Observing System Experiments using OFAM2, showing that all of the main components of the global ocean observing system are important for constraining an eddy-resolving ocean model. Oke et al. (2008) presented results using OFAM2 to show that when constrained by data assimilation, their model reproduced the variability around Australia with sea-level anomaly (SLA) errors of 6–12 cm and Sea-Surface Temperature (SST) errors of 0.5–0.9°C. Schiller et al. (2008) used results from the data assimilating version of OFAM2 to quantify the seasonal and interannual variability of the major currents in the Australian region and the Indonesian Throughflow. Using the same model, Schiller et al. (2010) showed that the deep-reaching sub-surface intraseasonal variability in the eastern Indian Ocean and the Indonesian Throughflow is closely linked with equatorial wind stress anomalies in the central Indian Ocean. Other applications of previous versions of OFAM include an investigation of a series of coral bleaching events in the Great Barrier Reef (Schiller et al., 2009), an analysis of eddy dynamics in the Tasman Sea (Oke and Griffin, 2011), an analysis of fronts in the Southern Ocean (Langlais et al., 2010), an investigation of the seasonality of Chlorophyll *a* in anti-cyclonic eddies off Western Australia (Dietze et al., 2009), and a climate downscaling (Sun et al., 2012). An operational version of OFAM2 is run at the Bureau of Meteorology and is described by Brassington et al. (2007).

The details of the model configuration are described in Sect. 2. An evaluation of the last 18 yr of a 32-yr model run is presented in Sect. 3, followed by a summary

and conclusions in Sect. 4. A comprehensive description of the technical details of the model configuration are described in Appendices A and B.

2 Model configuration

OFAM3 is a near-global, eddy-resolving, z^* configuration of version 4p1 of the Modular Ocean Model (Griffies, 2009), developed principally for the purpose of hindcasting and forecasting upper ocean conditions in non-polar regions. The key features of the configuration of OFAM3 are described here, and a comprehensive technical description of OFAM3, including model parameterisations, initial conditions, and forcing, is given in Appendix A. The model grid has $1/10^\circ$ grid spacing for all longitudes and between 75° S and 75° N, with 5-m vertical resolution down to 40-m depth and 10-m vertical resolution to 200-m depth. OFAM3 is forced with 1.5° -resolution, 3-hourly surface heat, freshwater, and momentum fluxes from ERA-interim (Dee and Uppala, 2009). Surface temperature is restored to monthly-averaged observations with a restoring time-scale of 10 days. Similarly, surface salinity is restored to monthly-averaged climatology with a restoring time-scale of 30 days. OFAM3 uses the mixed-layer model described by Chen et al. (1994). The model was initialised at rest, with zero sea-level, and with potential temperature and salinity from climatology, then integrated for 32 yr. The first 14-yr is the spin-up period, and the last 18-yr, spanning the period 1993–2010, are analysed in this study.

OFAM3 includes a BGC cycling model, called the Whole Ocean Model with Biogeochemistry and Trophic-dynamics (WOMBAT). A comprehensive description of WOMBAT, including parameterisations, initial conditions and forcing, is given in Appendix B. Briefly, WOMBAT is a three-dimensional NPZD (Nitrate, Phytoplankton, Zooplankton, Detritus) model described by Kidston et al. (2011), with the addition of the iron, oxygen, and carbon cycles. The iron, oxygen, and carbon cycles are linked to the nitrate uptake and remineralisation through a constant Redfield ratio, and the formation of calcium carbonate is a constant fraction of organic carbon production. The atmospheric

Evaluation of a near-global eddy-resolving ocean model

P. R. Oke et al.

[Title Page](#)

[Abstract](#)

[Introduction](#)

[Conclusions](#)

[References](#)

[Tables](#)

[Figures](#)

[⏪](#)

[⏩](#)

[◀](#)

[▶](#)

[Back](#)

[Close](#)

[Full Screen / Esc](#)

[Printer-friendly Version](#)

[Interactive Discussion](#)



and 58.5 m respectively – again with the model having deeper MLDs than observed. In general, in regions of strong convection (e.g., Weddell, Ross and Labrador Sea, and south-eastern Pacific) the model mixed layers are too deep. This may be due to limitations of the mixed-layer scheme used in OFAM3, and is an issue that will be considered in future versions of OFAM.

3.3 SST seasonal cycle

Here, we compare the seasonal cycle of the modelled SST with gridded $1/4^\circ$ -resolution satellite observations from AMSR-E (www.ssmi.com) and Reynolds et al. (2007). The zonally-averaged mean seasonal cycle from the model is shown in Fig. 3a, along with the difference between the modelled and observed seasonal cycle in Fig. 3b-c, and the time-averaged, zonally-average differences in Fig. 3d. The AMSR-E fields are 7-day averages and are based on data for the period 1/2003–12/2010; and the model and Reynolds fields are for the entire 18-yr model run (note that we restore OFAM3 to Reynolds SST). These comparisons demonstrate the seasonal cycle in the model is generally too weak. In each hemisphere at mid-latitude, the zonal averaged SST is 0.5 – 1.5°C too cold in summer, and 0.5 – 1.0°C too warm in winter. North of about 55°N , the AMSR-E SST is up to 2.5°C warmer than the model, and Reynolds SST is over 1.5° colder than the model. This indicates that north of 55°N , the observations are in disagreement. For most latitudes, the time-averaged, zonally-averaged SST in the model is within 0.5°C of observations.

3.4 Zonal-averaged fields

The time-mean and zonal average of modelled potential temperature and salinity are shown in Fig. 4, along with their differences from climatology. The time-mean and zonal average modelled potential temperature field (Fig. 4a) shows the expected broad-scale features, with warm water at shallow, low-latitudes, and cold waters over all depths at high-latitudes. The time-mean and zonal average modelled salinity (Fig. 4c) includes

Evaluation of a near-global eddy-resolving ocean model

P. R. Oke et al.

[Title Page](#)

[Abstract](#)

[Introduction](#)

[Conclusions](#)

[References](#)

[Tables](#)

[Figures](#)

[⏪](#)

[⏩](#)

[◀](#)

[▶](#)

[Back](#)

[Close](#)

[Full Screen / Esc](#)

[Printer-friendly Version](#)

[Interactive Discussion](#)



globally-averaged MOC shows that the maximum MOC in the Deacon cell is 39 Sv. These results are comparable to other model-based estimates (e.g., Maltrud and McClean, 2005; Kohl and Stammer, 2007; Doos et al., 2008), and to observational estimates in the North Atlantic (e.g., Cunningham et al., 2007).

3.5 El Niño-related indices

Time-series of the observed and modelled NINO1.2, NINO3, NINO4, and NINO3.4 anomalies are shown in Fig. 6. The observed indices are based on monthly-mean Reynolds SST (Reynolds et al., 2007). The biggest event in the time-series is the large positive anomaly in NINO1.2, NINO3 and NINO3.4, corresponding to the 1997 El Niño. This event is well reproduced by the model, with the correct phase and amplitude. The agreement between the modelled and observed NINO1.2, 3, 4 and 3p4 anomalies are excellent, with a correlation of 0.91, 0.96, 0.96, and 0.97 respectively, and an RMSD of 0.56, 0.38, 0.26, 0.32 °C respectively.

3.6 Volume transports

The time-mean modelled volume transports through well-defined straits and passages are listed in Table 1, along with observation-based estimates (where available) for each region. In each case, the observational estimates are based on some assumptions, either about the governing dynamics (e.g., geostrophy), level of no motion, or from interpolation and extrapolation of discrete observations. The modelled ACC transport is between about 144 Sv and 176 Sv. This is close to the observed range of 129 Sv and 157 Sv (Table 1; Rintoul and Sokolov, 2001; Cunningham et al., 2003). The modelled transports are 10–15 % stronger than observed estimates in Drake Passage and south of Tasmania.

The volume transport through the Indonesian Throughflow (ITF) passages include observational estimates from the INSTANT program (Gordon et al., 2010). The INSTANT estimates are for a 3-yr period, considerably shorter than the 18-yr model

Evaluation of a near-global eddy-resolving ocean model

P. R. Oke et al.

[Title Page](#)

[Abstract](#)

[Introduction](#)

[Conclusions](#)

[References](#)

[Tables](#)

[Figures](#)



[Back](#)

[Close](#)

[Full Screen / Esc](#)

[Printer-friendly Version](#)

[Interactive Discussion](#)



it appears that the model has greater variability than the observations, particularly away from the core EAC.

Other well-defined passages include the Florida Current (Hamilton et al., 2004) and the Mozambique Channel (DiMarco et al., 2002). We find that the modelled volume transport of the Florida Current is considerably less than observed. We suspect this is partially because of the decision to “fill in” a large portion of the Great Bahama Bank, as discussed in Appendix A. The volume transport of the modelled Mozambique Channel is within the broad range of observed estimates, and is consistent with other eddy-resolving and eddy-permitting models, as described by DiMarco et al. (2002).

3.7 RMS of SLA, SST, and Chlorophyll *a*

We compare maps of the root-mean-square (RMS) of SLA, SST anomaly (SSTA), and surface Chlorophyll *a* from the model and from observations in Figs. 8, 9 and 10.

3.7.1 Data description

The SLA comparisons are based on daily-mean modelled SLA and weekly maps of SLA on a $1/3^\circ$ grid, produced by Archiving, Validation, and Interpretation of Satellite Oceanographic (AVISO; Ducet et al., 2000). The SSTA comparisons are based on 7-day averaged modelled SSTA and 7-day averaged AMSR-E SSTA observations. The surface Chlorophyll *a* comparisons are between daily-mean model estimates (produced by converting surface phytoplankton to Chlorophyll *a*) and 8-day 9-km composite maps from SeaWiFS for 1997–2008.

The model SLA fields that underpin Fig. 8a are the model sea-level minus the model MSL (shown in Fig. 1a). The observed SLA fields are referenced to the CNES-CLS09 MSL (Fig. 1b) and tend to have larger errors near the coast associated with the correction for tides. The SSTA fields in Fig. 9 are anomalies from the seasonal cycle. So, for the RMS of the modelled (observed) SSTA, the seasonal cycle from the model (observations) is first removed from 7-day averaged model (observational) fields and the

Evaluation of a near-global eddy-resolving ocean model

P. R. Oke et al.

[Title Page](#)

[Abstract](#)

[Introduction](#)

[Conclusions](#)

[References](#)

[Tables](#)

[Figures](#)

[⏪](#)

[⏩](#)

[◀](#)

[▶](#)

[Back](#)

[Close](#)

[Full Screen / Esc](#)

[Printer-friendly Version](#)

[Interactive Discussion](#)



RMS of the resulting anomaly is computed. The observed AMSR-E SST fields tend to have larger errors near the coast, and have been excluded from the analysis presented in Fig. 9.

The evaluation of Chlorophyll *a* is more complicated than the assessment of SLA and SSTA for several reasons. Firstly, the conversion of modelled phytoplankton concentration (in Nitrogen units, mmol m^{-3}) to Chlorophyll *a* concentration (mg Chla m^{-3}) assumes a fixed ratio of C:Chla of 50 : 1 and C:N of 106 : 16, and is known to be an approximation (Taylor et al., 1997). Secondly, satellite-derived Chlorophyll *a* is based on estimates of the water leaving radiance that is sensitive to poorly known corrections of the atmosphere on radiances. Thirdly, satellite-derived Chlorophyll *a* tends to be under-estimated in the Southern Ocean (Clementson et al., 1998), and over-estimated near the coast and sea-ice because of the influence of dissolved organic matter and sediment resuspension (Moore et al., 2007). Finally, the nominal uncertainty in the SeaWiFS and MODIS estimates of Chlorophyll *a* in the open ocean water is $\pm 25\text{--}35\%$ (Behrenfeld et al., 2006; Moore et al., 2009). Because of these uncertainties in the observations, we focus our BGC evaluation on assessing the spatial patterns of the modelled and observed Chlorophyll *a* variability.

3.7.2 SLA comparisons

The SLA comparison (Fig. 8) generally shows excellent agreement between the model and observations, with the model reproducing almost all of the local maxima in the observations. The SLA variability is high along the path of the ACC, with good agreement between the model and the observations regarding the location and magnitude of local maxima there. There is also relatively high SLA variability in both the model and the observations in the Indian Ocean, around 25°S and 12°S ; off the coast of Somalia; in the Western Pacific, off Papua New Guinea and Taiwan; and in the central and eastern Pacific at around $5\text{--}10^\circ\text{N}$. The highest SLA variability is in the WBC regions. These regions are discussed in more detail below.

Evaluation of a near-global eddy-resolving ocean model

P. R. Oke et al.

[Title Page](#)

[Abstract](#)

[Introduction](#)

[Conclusions](#)

[References](#)

[Tables](#)

[Figures](#)



[Back](#)

[Close](#)

[Full Screen / Esc](#)

[Printer-friendly Version](#)

[Interactive Discussion](#)



and McClean, 2005; van Sebille et al., 2012) and $1/4^\circ$ -resolution (e.g., Biastoch et al., 2009) models.

The modelled and observed RMS for SLA in the EAC region (Fig. 8) shows good agreement, with a local maximum at about 33° S, 154° E. The magnitude of the modelled SLA variability at this maximum, off south-eastern Australia, is less than observed. Conversely, the model shows high SLA variability at about 25° S and east of 160° E. This feature appears further east in the observations, but with a smaller magnitude. It's possible that the higher-than-observed SLA variability in this region acts to dissipate energy from the South Equatorial Current that is "feeding" the EAC. This could partly explain why the variability of SLA south of the EAC separation point is less than observed.

In the BMC region, the SLA has high variability over a C-shaped region, around a local minima at about 45° W, 45° S; with a local maximum at about 50° W, 42° S. The BMC region also has a local maximum in SLA variability along a path extending from Drake Passage. The location of the local SLA variability maximum at the confluence of the Brazil and Malvinas Currents is mis-placed by about 1–2 degrees in the model, compared to the observations. This displacement is consistent with the systematic differences in the modelled and observed MSL (Fig. 1), indicating that the mean flow and the associated variability is displaced by a degree or two in the model compared to observations.

3.7.3 SST anomaly comparisons

The SSTA comparisons (Fig. 9) demonstrate that the model reproduces most of the observed local maxima in the RMS of SSTA. In regions where the SST variability is relatively low (e.g., between $5\text{--}25^\circ$ N and between 130° E and 140° W in the Pacific Ocean) the modelled SSTA is less than the observations by about $0.25\text{--}0.5^\circ$ C. O'Carroll et al. (2008) suggested that the RMS of the measurement error of AMSR-E SST is about 0.42° C. This indicates that in the regions where the SSTA variability is small (between $0.5\text{--}0.7^\circ$ C), the signal in the observations is likely to be dominated by measurement

Evaluation of a near-global eddy-resolving ocean model

P. R. Oke et al.

[Title Page](#)

[Abstract](#)

[Introduction](#)

[Conclusions](#)

[References](#)

[Tables](#)

[Figures](#)



[Back](#)

[Close](#)

[Full Screen / Esc](#)

[Printer-friendly Version](#)

[Interactive Discussion](#)



error because the signal-to-noise ratio is low. So the lower-than-observed variability in the model may be an over-estimate in the observed RMS, rather than an under-estimate in the model. Conversely, where the SSTA variability is high (e.g., in the WBC regions), the modelled SSTA is generally greater than the observed SSTA (Fig. 9).

5 3.7.4 Chlorophyll *a* comparisons

In a broad sense the modelled and “observed” Chlorophyll *a* variability (Fig. 10) shows similar patterns of high variability at high latitudes, and low variability in the oligotrophic gyres. There are clearly large discrepancies between the modelled and observed surface Chlorophyll *a* fields in many regions. In part, this is because the observed Chlorophyll *a* includes the impacts of mechanisms that are not included in the model, including iron fertilisation from sediments and sea-ice melt. The biggest differences in Fig. 10 are adjacent to continental shelves and along the sea-ice edge, where the observed variability includes variability associated with processes not represented in the model. Within the interior of each ocean gyre, the model tends to have more variability in Chlorophyll *a* than observed. This may be due to the systematic errors in the model’s MLD – with the model generally showing mixed layers that are too deep. This means that the model tends to entrain more sub-surface nutrients into the euphoric layers of the ocean, “stimulating” phytoplankton growth at higher levels than observed. This difference may also be a limitation of a BGC model with a single phytoplankton class - and may be improved if multiple size classes were used (Follows et al., 2007; Baird and Suthers, 2007). By contrast, the model shows weaker variability in regions where wind-driven upwelling is prevalent (e.g., Canary Current, Peru/Chile Current, US West coast, Indonesian coast), probably due to limitations in horizontal and vertical resolution.

3.7.5 Relating SLA, SST, and Chlorophyll *a* comparisons

25 The RMS of modelled and observed SLA, SSTA, and Chlorophyll *a* (Figs. 8, 9 and 10) show regions of high variability in all WBC regions. However, on a broad scale, it

Evaluation of a near-global eddy-resolving ocean model

P. R. Oke et al.

[Title Page](#)

[Abstract](#)

[Introduction](#)

[Conclusions](#)

[References](#)

[Tables](#)

[Figures](#)



[Back](#)

[Close](#)

[Full Screen / Esc](#)

[Printer-friendly Version](#)

[Interactive Discussion](#)



Evaluation of a near-global eddy-resolving ocean model

P. R. Oke et al.

[Title Page](#)

[Abstract](#)

[Introduction](#)

[Conclusions](#)

[References](#)

[Tables](#)

[Figures](#)

[⏪](#)

[⏩](#)

[◀](#)

[▶](#)

[Back](#)

[Close](#)

[Full Screen / Esc](#)

[Printer-friendly Version](#)

[Interactive Discussion](#)

appears that the location of the maxima in the RMS fields is different for each variable. The maxima in the RMS of SST and Chlorophyll *a* occur at the latitude of the strongest meridional gradient. The SSTA maxima in the Kuroshio, Gulf Stream, Agulhas, and EAC regions are at higher latitudes than the SLA maxima. This is because there is a large signal in SSTA associated with the intersection of the quasi-isothermal, warm WBC waters with colder higher-latitude waters. Because the WBC flow is generally poleward, the SSTA maxima are poleward of the SLA maxima. This characteristic is less clear in the BMC region, probably because the northward flow of the Malvinas Current, east of Argentina, advects the colder ACC waters northward into the path of the warmer Brazil Current, as well as vice-versa. As a result, the maxima in SLA and SSTA in the BMC region are more closely co-located. The modelled Chlorophyll *a* maximum in each WBC region is generally equatorward, and sometimes eastward, of the SLA maximum. In each basin, the mean Chlorophyll *a* has a maximum at around 40° N and S (not shown) – and the maximum for the RMS of the modelled Chlorophyll *a* is on the poleward edge of this maximum. We suspect that the maximum in the RMS Chlorophyll *a* field is due to the confluence of the high Chlorophyll *a* waters around 40° N and S, towards the center of each gyre, with the low-Chlorophyll *a* waters of each WBC.

At mid-southern latitudes, there is high SLA and SSTA variability (Figs. 8 and 9) in both the model and observations in the Leeuwin Current region, and between 20–30° S across the Indian Ocean. In the tropics, both the model and observations show high SLA and SSTA variability to the west of the Indonesian Throughflow region between about 8–12° S that is most likely associated with seasonal Rossby waves (Masumoto and Meyers, 1998) – though the modelled SSTA does not show the high variability that is evident in the observations, as discussed above. Both the model and observations show high SLA and SSTA variability associated with the Great Whirl off Somalia, where a corresponding maximum in Chlorophyll *a* variability is evident in the observations and (to a lesser extent) the model. Broad regions of high SLA variability, associated with instabilities originating in the Kuroshio Current to the east of the Philippines (~ 10° N) and east of Taiwan (~ 22° N) are evident in both the model and the observations. High

SLA variability is evident in the Gulf of Mexico, associated with the Loop Current, in both the model and observations, coincident with a local maximum in SSTA.

There are two zonal bands of high SLA variability (Fig. 8) in the central and eastern tropical Pacific, at about 5° N and 10° N that are associated with the North Equatorial Current and the North Equatorial Counter Current respectively. The SSTA field (Fig. 9) show maxima in the Pacific Ocean along the equator, extending from the coast of South America to about 150–160° E. In the same region, the Chlorophyll *a* fields show high variability along the equator. These features are evident in both the model and observations, although the modelled SLA and SSTA variability is weaker than observed, and the modelled Chlorophyll *a* variability is higher than observed.

3.8 Snap-shots of Chlorophyll *a*

We include a qualitative assessment of the BGC in each WBC region by showing a series of “snap-shots” of modelled surface phytoplankton (Fig. 11) and satellite-derived Chlorophyll *a* from MODIS (Fig. 12). Due to the chaotic nature of the mesoscale circulation, and the lack of data assimilation in the model, we do not expect to see one-to-one agreement between the model and observations. Rather, we expect to see evidence of similar types of features, on similar spatial scales in these fields.

In all regions shown in Figs. 11 and 12 phytoplankton and Chlorophyll *a* fields show features that are clearly associated with eddies, meanders, and high-nutrient filaments. The model velocity field at 50 m depth is overlaid on the model fields to show the nature of the circulation. Strong biophysical coupling is evident in all regions the Kuroshio region, with mesoscale signals evident in both the model and observations; the Gulf of Mexico, with high BGC activity around the periphery of the Loop Current; in the Agulhas region, with evidence of small-scale mesoscale variability – on scales of a few degrees, in both the modelled phytoplankton and the observed Chlorophyll *a* ; in the confluence of Malvinas and Brazil Currents, with strong features associated with the intersection of different water masses; and in the EAC region, with the signature of mesoscale eddies and meanders evident in both the model and observations.

Evaluation of a near-global eddy-resolving ocean model

P. R. Oke et al.

[Title Page](#)

[Abstract](#)

[Introduction](#)

[Conclusions](#)

[References](#)

[Tables](#)

[Figures](#)



[Back](#)

[Close](#)

[Full Screen / Esc](#)

[Printer-friendly Version](#)

[Interactive Discussion](#)



Evaluation of a near-global eddy-resolving ocean model

P. R. Oke et al.

[Title Page](#)

[Abstract](#)

[Introduction](#)

[Conclusions](#)

[References](#)

[Tables](#)

[Figures](#)

[⏪](#)

[⏩](#)

[◀](#)

[▶](#)

[Back](#)

[Close](#)

[Full Screen / Esc](#)

[Printer-friendly Version](#)

[Interactive Discussion](#)

to over-estimate the magnitude of SST anomalies in regions of high variability, such as WBC regions. Analyses of the model's MSL, MLD, volume transports through key straits and passages, zonal-averaged temperature, salinity and MOC lead us to conclude that the model average state is realistic; and that the model realistically represents the variability in the upper ocean and at intermediate depths. Nevertheless, a few systematic errors are evident in the model. For example, the modelled mixed layer is generally too deep in mid-latitudes, and in some regions (e.g., the Brazil-Malvinas Confluence) the modelled variability is along a different path to that observed from altimetry. The impact of these errors is evident on the modelled BGC fields that are evaluated here by comparisons with satellite observations. We find that the variability of the modelled Chlorophyll *a* is generally too high – a characteristic that we attribute (in part) to the model's systematic errors in MLD. Despite these systematic errors, we have shown that the modelled variability is generally realistic; and we conclude that the model variability is suitable for further analysis to better understand ocean dynamics, variability, teleconnections and so on.

The next step for OFAM3 is the performance of a 20-yr ocean reanalysis (with data assimilation), similar to that described by Oke et al. (2005, 2008) and Schiller et al. (2008). Subsequent to that activity, OFAM3 is intended to be used in the next generation of the operational ocean forecast system at the Australian Bureau of Meteorology. The next phase of technical developments of the OFAM model will likely include the development of a truly global model, including the Arctic Ocean with coupling to a sea-ice model. Other planned developments include the adoption of bulk surface heat fluxes, instead of prescribed fluxes, and the application of an atmospheric boundary layer model. We expect that these developments will help address some of the shortcomings identified in this study.

Appendix A

OFAM3

A1 Resolution

OFAM3 is a near-global (i.e., non-Arctic) eddy-resolving configuration of version 4p1 of the Modular Ocean Model (Griffies, 2009, December 2009 release), developed principally for the purpose of hindcasting and forecasting upper ocean conditions in non-polar regions. The model grid has $1/10^\circ$ grid spacing for all longitudes and between 75° S and 75° N ($\sim 8\text{--}11$ km \times 11 km) and is comprised of 3600×1500 grid points. The vertical model coordinate is z^* (Griffies, 2009), with 51 vertical levels, with resolution grading from 5 m at the surface to 10 m between 100 and 200 m depth, then 120 m at 1000 m, and eventually 1000 m near the sea floor. Also, we use partial grid cells (Adcroft et al., 1997) to improve the representation of topography (to reduce the stepiness) and to improve the vertical resolution near the bottom. We set the minimum height for each partial cell to be no less than 5 m or 20% of the full cell height, whichever is greater ($\Delta z_{\text{partial}} > \max(5 \text{ m}, 0.2 \times \Delta z_{\text{full}})$).

A2 Topography

The topography for OFAM3 is derived from the 30 arc-second GEBCO_08 topography (www.bodc.ac.uk/data/online_delivery/gebco/) for most of the world, and a 9 arc-second topography produced by Geoscience Australia (Whiteway, 2009). The minimum number of vertical levels in the model is 3, so the minimum depth in the model is 15 m. In regions where the real topography is less than 15 m, the model topography is set to either zero (i.e., land), or to 15 m. Often the decision to “fill in” or “dig out” a grid cell is subjective. In some cases (e.g., Torres Strait, Indonesian Straits) some points are filled in, and others dug out so that the correct cross-sectional area of a Strait is preserved. In other areas where a broad region is shallow, large areas are sometimes filled in

Evaluation of a near-global eddy-resolving ocean model

P. R. Oke et al.

[Title Page](#)

[Abstract](#)

[Introduction](#)

[Conclusions](#)

[References](#)

[Tables](#)

[Figures](#)



[Back](#)

[Close](#)

[Full Screen / Esc](#)

[Printer-friendly Version](#)

[Interactive Discussion](#)



with land (e.g., Great Bahama Bank), and sometimes set to the minimum depth (e.g., Southern Persian Gulf). Additionally, some inland, or regional seas are replaced with land either because they are out of the scope for planned applications of this model (e.g., Caspian Sea; Sea of Azov), to avoid problems with computational stability, or to avoid problems with the northern boundary (e.g., Laptev Sea, Kara Sea).

A3 Forcing

OFAM3 is forced with 1.5°-resolution, 3-hourly surface heat, freshwater, and momentum fluxes from ERA-interim (Dee and Uppala, 2009). The surface heat flux is applied to the top model layer for components associated with the latent, sensible and long-wave heat flux. The penetrating short-wave heat flux is applied over multiple model-levels according to a single exponential decay law, with penetration depths based on SeaWIFS Kd-490. The model forcing includes climatological, seasonal river forcing estimated by Dai and Trenberth (2002) and Dai et al. (2009). River forcing is applied as a water flux, with the injection of zero-salinity water and local SST distributed over the top 3 model layers at coastal grid points. Surface temperature and salinity are relaxed to monthly-averaged Reynolds SST (Reynolds et al., 2007) and monthly-averaged CARS salinity (CSIRO Atlas of Regional Seas, released in 2009; Ridgway and Dunn, 2003) with a restoring time-scale of 10 days and 30 days, respectively. The impact of variability in the Arctic Ocean is included by restoring the temperature and salinity over all depths within 1 degree of the northern boundary to monthly averaged fields from version 2.1.6 of the Simple Ocean Data Assimilation (SODA; Carton et al., 2000; Carton and Giese, 2008, accessed on October 2010) between 1993 and 2008, using a restoring timescale of 30 days. After 2008, we restore to a seasonal climatology based on SODA. Meridional velocities at the northern and southern boundaries are zero, with a no-slip condition for zonal velocities. To avoid any significant drift in the deep ocean fields, the temperature and salinity are restored to CARS climatology below 2000 m with a restoring time-scale of 365 days.

**Evaluation of a
near-global
eddy-resolving ocean
model**

P. R. Oke et al.

[Title Page](#)

[Abstract](#)

[Introduction](#)

[Conclusions](#)

[References](#)

[Tables](#)

[Figures](#)



[Back](#)

[Close](#)

[Full Screen / Esc](#)

[Printer-friendly Version](#)

[Interactive Discussion](#)



Evaluation of a near-global eddy-resolving ocean model

P. R. Oke et al.

[Title Page](#)

[Abstract](#)

[Introduction](#)

[Conclusions](#)

[References](#)

[Tables](#)

[Figures](#)

[⏪](#)

[⏩](#)

[◀](#)

[▶](#)

[Back](#)

[Close](#)

[Full Screen / Esc](#)

[Printer-friendly Version](#)

[Interactive Discussion](#)

A4 Initialisation and integration

The model was initialised at rest, with zero sea-level, and with potential temperature and salinity from a global version of CARS (Ridgway and Dunn, 2003). The model was spun-up for 14 yr, spanning the period 1993–2005, with time-varying forcing, as described above. The temperature, salinity, sea-level, and velocity fields at the end of 2005 were used as initial conditions for a second run spanning the period 1993–2010. The analyses presented in this paper are based on model years 14–32, spanning the period 1993–2010, and excludes the initial 14-yr spin-up period.

A5 Numerics

The time step is 540 s for model tracers, and 6 s for sea-level and depth-integrated velocities. A staggered forward time-step is used for tracers and velocity (Griffies, 2004, Sect. 12.6). The model time-step is typically limited by vertical velocities at about 200 m depth. A third-order Adams-Bashforth scheme is used for velocity advection, and a third-order upwind biased scheme is used for tracers (Hundsdoerfer and Trompert, 1994), in conjunction with a flux limiter scheme (Sweby, 1984). A predictor-corrector time-filter is also applied to sea-level using a non-dimensional damping parameter of $\gamma = 0.2$, as recommended by Griffies (2004, Sect. 12.7).

A6 Mixing parameterisations

OFAM3 uses the mixed-layer model described by Chen et al. (1994). The background vertical diffusivity and viscosity are 1×10^{-5} and $1 \times 10^{-4} \text{ m}^2 \text{ s}^{-1}$, respectively. The enhanced vertical diffusivity and viscosity due to shear instabilities are 2.5×10^{-3} and $5 \times 10^{-3} \text{ m}^2 \text{ s}^{-1}$, respectively. Additional vertical mixing is applied over the water column to represent the mixing effects of tides following Lee et al. (2006) (using a Munk-Anderson-P and Munk-Anderson-Sigma parameter of 0.25 and 3.0, respectively). This results in stronger mixing in regions of large-amplitude tides, such as the north-west of

Australia. The tidal mixing coefficients depend on spatially resolved, but time invariant estimates of tidal amplitudes that are obtained from a global inverse model (Egbert et al., 1994).

A convective adjustment is applied every time step using fully explicit mixing when the water column becomes unstable. The explicit horizontal diffusion is zero. Horizontal viscosity is resolution- and state-dependent using a biharmonic Smagorinsky viscosity scheme (Griffies and Hallberg, 2000), with an isotropic parameter of 3.0 and an anisotropic parameter of 3.0.

A7 Volume conservation

OFAM3 is configured to be volume-conserving (z^*). Thermal expansion is therefore not included in the model. As a result, the thermostatic component of observed sea-level rise that is evident in observations (e.g., Church and White, 2006) is not reproduced in OFAM3. However, the global-averaged sea-level of the simulated ocean is sensitive to any imbalance between the prescribed precipitation, evaporation, and river forcing. The global-averaged net freshwater flux from ERA-Interim (Dee and Uppala, 2009) is not zero. We find that the annual- and global-averaged evaporation always exceeds precipitation (and river forcing), so we apply a very small spatially uniform precipitation – a “drizzle” – that is fixed for each year of the spin-up run so that the net volume flux is zero. A similar approach was used by Balmaseda et al. (2008) for a coarse-resolution global ocean reanalysis and seasonal prediction system. The mean annual “drizzle” that is applied accounts for a sea-level change of 0.06 m yr^{-1} . For comparison, the mean annual sea-level change due to the other components of the freshwater budget is -1.31 m yr^{-1} for evaporation; 0.43 m yr^{-1} for large-scale precipitation; 0.72 m yr^{-1} for convective precipitation; and 0.1 m yr^{-1} for river run-off. The model is not intended for studies of sea-level rise, so it does not include forcing from glacial melt.

Time series of the area-weighted global-mean sea-level from the model and from observations are shown in Fig. 13. By design, the model does not have a trend in the global-mean sea-level, but the time-mean of -1.8 cm has been removed from the

Evaluation of a near-global eddy-resolving ocean model

P. R. Oke et al.

[Title Page](#)

[Abstract](#)

[Introduction](#)

[Conclusions](#)

[References](#)

[Tables](#)

[Figures](#)

[⏪](#)

[⏩](#)

[◀](#)

[▶](#)

[Back](#)

[Close](#)

[Full Screen / Esc](#)

[Printer-friendly Version](#)

[Interactive Discussion](#)



model. The time-mean of 1.6 cm and the linear trend of 0.29 cm yr^{-1} have been removed from the observations. The seasonal fluctuations of the global-averaged sea-level have a magnitude of between 1 and 2 cm, in agreement with the observations, in both phase and amplitude. Because a greater area of the southern (northern) hemisphere is covered by ocean (land), the global mean sea-level has a minimum in late-austral summer – owing to evaporation over the Southern Hemisphere and snow accumulation over the Northern Hemisphere.

Appendix B

WOMBAT

Details of the ocean biogeochemical (BGC) processes included in the Whole Ocean Model of Biogeochemistry And Trophic-dynamics (WOMBAT) model are described below. This model is based on a NPZD (Nutrient, Phytoplankton, Zooplankton and Detritus) model with the addition of bio-available iron limitation (Fe), dissolved inorganic carbon (DIC), calcium carbonate (CaCO_3), alkalinity (ALK), and oxygen (O). In this model we have one class each of photoplankton and zooplankton. These are calculated on the same grid as temperature.

The following equations parameterise the biogeochemical transformations between the various BGC state variables of WOMAT with the BGC model parameters summarised in Table 2. In addition to these BGC transformations, the BGC state variables are transported around the ocean using the same physical equations as used for T and S . For Fe, DIC and Oxygen in the surface layer, there are also air-sea flux terms which are discussed below.

GMDD

5, 4305–4354, 2012

Evaluation of a near-global eddy-resolving ocean model

P. R. Oke et al.

[Title Page](#)

[Abstract](#)

[Introduction](#)

[Conclusions](#)

[References](#)

[Tables](#)

[Figures](#)

[⏪](#)

[⏩](#)

[◀](#)

[▶](#)

[Back](#)

[Close](#)

[Full Screen / Esc](#)

[Printer-friendly Version](#)

[Interactive Discussion](#)



Evaluation of a near-global eddy-resolving ocean model

P. R. Oke et al.

[Title Page](#)

[Abstract](#)

[Introduction](#)

[Conclusions](#)

[References](#)

[Tables](#)

[Figures](#)

[⏪](#)

[⏩](#)

[◀](#)

[▶](#)

[Back](#)

[Close](#)

[Full Screen / Esc](#)

[Printer-friendly Version](#)

[Interactive Discussion](#)

$$\frac{dP}{dt} = \bar{J}(z, t, T, N, \text{Fe})P - G(P, Z) - \mu_P P \quad (\text{B1})$$

$$\frac{dZ}{dt} = \gamma_1 G(P, Z) - \gamma_2 Z - \mu_Z Z^2 \quad (\text{B2})$$

$$\frac{dD}{dt} = (1 - \gamma_1)G(P, Z) + \mu_Z Z^2 - \mu_D D - w_D \frac{dD}{dz} \quad (\text{B3})$$

$$\frac{dN}{dt} = \mu_D D + \gamma_2 Z + \mu_P P - \bar{J}(z, t, T, N, \text{Fe})P \quad (\text{B4})$$

$$\frac{d\text{Fe}}{dt} = 0.02 \frac{dN}{dt} - \tau_{\text{scav}} \max(0, \text{Fe} - 0.6) \quad (\text{B5})$$

Equation (B1) describes phytoplankton growth ($\bar{J}(z, t, T, N, \text{Fe})P$), loss due to zooplankton grazing ($G(P, Z)$), and phytoplankton mortality ($\mu_P P$). Phytoplankton growth rate is a function of temperature (T), light (I) and nutrient concentration (N and Fe) and the growth rate is given by:

$$\bar{J}(z, t, T, N, \text{Fe}) = J_{\max}(T) \times \min \left[\frac{J(z, t, T)}{J_{\max}(T)}, \frac{N}{N + k_N}, \frac{\text{Fe}}{\text{Fe} + k_{\text{Fe}}} \right] \quad (\text{B6})$$

$$J(z, t, T) = J_{\max}(T) \left(1 - \exp \left(\frac{-aI(z, t)}{J_{\max}(T)} \right) \right) \quad (\text{B7})$$

$$I(z, t) = \text{PAR} \times I(0, t) \times \text{Frac}(z) \quad (\text{B8})$$

$$J_{\max}(T) = ab^{cT} \quad (\text{B9})$$

where J_{\max} is the maximum phytoplankton growth at a given T , assuming no light or nutrient limitation; $J(z, t, T)$ is the impact of light on growth rate, and is based on Westwood et al. (2011), PAR is the photosynthetically available radiation, $I(0, t)$ is the time-varying incident solar radiation at the surface, and $\text{Frac}(z)$ is the light attenuation that is obtained from a single exponential decay law, with penetration depths based on SeaWiFS K_d -490 (which was the same as the value used by the Chen et al. (1994) mixing scheme).

Equation (B2) describes the zooplankton, represented as the balance between growth due to phytoplankton grazing ($G(P, Z)$) and losses due to zooplankton excretions ($\gamma_2 Z$) and mortality ($\mu_Z Z^2$). The grazing of phytoplankton by zooplankton ($G(P, Z)$) is given by:

$$G(P, Z) = \frac{g\epsilon P^2}{g + \epsilon P^2} Z, \quad (\text{B10})$$

where γ_1 is the efficiency of zooplankton grazing on phytoplankton, while the remainder becomes detritus.

Equation (B3) describes the detritus field, and includes input from zooplankton grazing and mortality, as well as terms for detrital decomposition ($\mu_D D$) and sinking ($w_D \frac{dD}{dz}$). The sinking term transports detritus vertically downward through the water column. In the deep ocean detritus remineralises back into inorganic form, completing the nutrient cycle.

Equation (B4) describes the nutrient (Nitrate) field that is controlled by physical supply (upwelling and vertical mixing) and phytoplankton growth rate and remineralization. We assume a Redfield Ratio of 16 : 106 : 172 (N:C:O₂) with carbon and oxygen and hence we do not include nitrification or denitrification processes or atmosphere deposition. In this way Nitrate is analogous to phosphate.

An additional source of limitation on phytoplankton growth rate is iron (Fe) that is described by Eq. (B5). Iron is supplied to the ocean by dust deposition at the surface (Mongin et al., 2011) and from sediments where the depth is less than 200 m (Mongin et al., 2009). Changes in iron are related to nitrate uptake, using a molar ratio for Fe : N of $2.0 \times 10^{-5} : 1$ (Christian et al., 2002), and iron is scavenged when it has a concentration $> 0.6 \mu\text{mol m}^{-3}$, which works to maintain the deep ocean iron concentration at this value (Archer and Johnson, 2000). Calcium carbonate (CaCO₃) production is fixed at 8 % of particulate organic carbon production (Yamanaka and Tajika, 1996), and is given by:

Evaluation of a near-global eddy-resolving ocean model

P. R. Oke et al.

[Title Page](#)[Abstract](#)[Introduction](#)[Conclusions](#)[References](#)[Tables](#)[Figures](#)[⏪](#)[⏩](#)[◀](#)[▶](#)[Back](#)[Close](#)[Full Screen / Esc](#)[Printer-friendly Version](#)[Interactive Discussion](#)

$$\frac{d\text{CaCO}_3}{dt} = \frac{0.08 \times 106}{16} \left((1 - \gamma_1)G(P, Z) + \mu_Z Z^2 \right) - \mu_{\text{CaCO}_3} \text{CaCO}_3 - w_{\text{CaCO}_3} \frac{d\text{CaCO}_3}{dz} \quad (\text{B11})$$

$$\frac{d\text{O}_2}{dt} = -\frac{172}{16} \frac{dN}{dt} \quad (\text{B12})$$

$$\frac{d\text{DIC}}{dt} = \frac{106}{16} \frac{dN}{dt} - \frac{d\text{CaCO}_3}{dt} \quad (\text{B13})$$

$$\frac{d\text{ALK}}{dt} = -\frac{dN}{dt} - 2 \frac{d\text{CaCO}_3}{dt} \quad (\text{B14})$$

5 In the model we include two DIC tracers, represented here by Eq. (B13) for the natural and anthropogenic DIC. These two DIC tracers only differ in the atmospheric CO₂ concentration used in the air-sea flux calculation. For the natural DIC the atmospheric CO₂ was set to 280 ppm while for anthropogenic DIC the atmospheric CO₂ increases according to observations. At the surface we calculated the air-sea exchange of the two carbon tracers and oxygen following Lenton and Matear (2007), which uses the partial difference pressures between the ocean and atmosphere, the seasonal climatology of sea-ice concentrations, and the wind-speed squared and temperature dependent gas exchange coefficient. The initial conditions for N and O₂ are derived by the 2005 version of the World Ocean Atlas (WOA2005; Garcia et al., 2006a,b). Chlorophyll was taken from a climatology of SeaWiFS (1997–2008) and then scaled to N to initialise phytoplankton in the top 100 m, using the ratio N:Chla = 1 mmol m⁻³ N: 1.59 mg m⁻³ Chla) Zooplankton (Z) was initially estimated to be 0.05 of the initial phytoplankton concentration. The initial field for Fe was taken from a 500-yr integration of a coarser resolution simulation with the same BGC module. Preindustrial DIC was initialised from GLODAP (Key et al., 2004). To generate the annual mean fields of DIC and ALK for the nominal year 1997 we started with the observed climatology of Takahashi et al. (2009) from the year 2000, and then calculated ALK and DIC following (Lenton et al., 2012) using the annual mean sea surface and salinity from WOA2005 from Locarnini et al. (2006) and Antonov et al. (2006) respectively. To correct the DIC to 1997 we used the observed

Evaluation of a near-global eddy-resolving ocean model

P. R. Oke et al.

[Title Page](#)
[Abstract](#)
[Introduction](#)
[Conclusions](#)
[References](#)
[Tables](#)
[Figures](#)




[Back](#)
[Close](#)
[Full Screen / Esc](#)
[Printer-friendly Version](#)
[Interactive Discussion](#)


global atmospheric growth rate from Mauna Loa (Earth System Research Laboratory, 2009) and the approximation of the Revelle Factor (Sarmiento and Gruber, 2006). We then calculated the difference in the surface between our calculated DIC and ALK, and GLODAP DIC and ALK (Key et al., 2004), and corrected the entire water column based on this surface difference.

To assess the variability of the modelled phytoplankton, we convert it to Chlorophyll *a* (using a 1 : 1.59 ratio as described above), and compare it to Chlorophyll *a* estimates from SeaWIFS. We show the RMS of the model-derived Chlorophyll *a* and satellite-derived Chlorophyll *a* from SeaWIFS in Fig. 10, and a series of “snap-shots” of modelled phytoplankton and satellite-derived Chlorophyll *a* from MODIS in Fig. 12. These comparisons involve several assumptions and several limitations. The satellite measurements include the impacts of mechanisms that are not included in the model, including iron fertilisation from sediments and sea-ice melt. Also, the conversion of modelled phytoplankton concentration to Chlorophyll *a* concentration involves several assumptions, as described in Sect. 3.7.1.

Acknowledgements. Funding for this research was provided by CSIRO, through the Wealth from Oceans National Research Flagship, and through the Royal Australian Navy. The authors gratefully acknowledge comments from P. Sakov that led to improvements in this manuscript. Satellite altimetry is provided by NASA, NOAA and CNES. SST observations are provided by NOAA (www.nodc.noaa.gov) and Remote Sensing Systems (www.remss.com).

References

- Adcroft, A., Hill, C., and Marshall, L.: Representation of topography by shaved cells in a height coordinate ocean model, *Mon. Wea. Rev.*, 125, 2293–2315, 1997. 4324
- Antonov, J. I., Locarnini, R. A., Boyer, T. P., Mishonov, A. V., and Garcia, H. E.: World Ocean Atlas 2005, Volume 2: Salinity, in: NOAA Atlas NESDIS, edited by: Levitus, S., 182 pp., U.S. Government Printing Office, Washington, D.C., 2006. 4331
- Archer, D. E. and Johnson, K.: A Model of the iron cycle in the ocean, *Global Biogeochem. Cy.*, 14, 269–279, 2000. 4330

Evaluation of a near-global eddy-resolving ocean model

P. R. Oke et al.

[Title Page](#)

[Abstract](#)

[Introduction](#)

[Conclusions](#)

[References](#)

[Tables](#)

[Figures](#)



[Back](#)

[Close](#)

[Full Screen / Esc](#)

[Printer-friendly Version](#)

[Interactive Discussion](#)



Evaluation of a near-global eddy-resolving ocean model

P. R. Oke et al.

[Title Page](#)

[Abstract](#)

[Introduction](#)

[Conclusions](#)

[References](#)

[Tables](#)

[Figures](#)

[⏪](#)

[⏩](#)

[◀](#)

[▶](#)

[Back](#)

[Close](#)

[Full Screen / Esc](#)

[Printer-friendly Version](#)

[Interactive Discussion](#)



- Baird, M. E. and Suthers, I. M.: A size-resolved pelagic ecosystem model, *ecological modelling*, 203, 185–203, doi:10.1016/j.ecolmodel.2006.11.025, 2007. 4319
- Balmaseda, M. A., Vidard, A., and Anderson, D. L. T.: The ECMWF ocean analysis system: ORA-S3, *Mon. Wea. Rev.*, 136, 3018–3034, doi:10.1175/2008MWR2433.1, 2008. 4327
- 5 Behrenfeld, M. J., O'Malley, R. T., Siegel, D. A., McClain, C. R., Sarmiento, J. L., Feldman, G. C., Milligan, A. J., Falkowski, P. G., and Letelier, R. M.: Climate-driven trends in contemporary ocean productivity, *Nature*, 444, 752–755, 2006. 4316
- Biastoch, A., Böning, C. W., Scheinert, M., and Lutjeharms, J. R. E.: The Agulhas System as a Key Region of the Global Oceanic Circulation, in: *High Performance Computing in Science and Engineering '08*, edited by: Nagel, W. E., Kröner, D. B., and Resch, M. M., 459–469, Springer Berlin Heidelberg, 2009. 4318
- 10 Brassington, G. B., Pugh, T. F., Spillman, C., Schulz, E., Beggs, H., Schiller, A., and Oke, P. R.: BLUElink development of operational oceanography and servicing in Australia, *J. Res. Pract. Inf. Tech.*, 39, 151–164, 2007. 4307
- 15 Carton, J., Chepurin, G., and Cao, X.: A Simple Ocean Data Assimilation analysis of the global upper ocean 1950-95. Part II: Results, *J. Phys. Oceanogr.*, 30, 311–326, 2000. 4325
- Carton, J. A. and Giese, B. S.: A reanalysis of ocean climate using Simple Ocean Data Assimilation (SODA), *Mon. Wea. Rev.*, 136, 2999–3017, 2008. 4325
- Chelton, D. B., Gaube, P., Schlax, M. G., Early, J. J., and Samelson, R. M.: The influence of nonlinear mesoscale eddies on near-surface oceanic chlorophyll, *Science*, 334, 328–332, doi:10.1126/science.1208897, 2011. 4322
- 20 Chen, D., Rothstein, L., and Busalacchi, A.: A hybrid vertical mixing scheme and its application to tropical ocean models, *J. Phys. Oceanogr.*, 24, 2156–2179, 1994. 4308, 4326, 4329
- Christian, J. R., Verschell, M. A., Murtugudde, R., Busalacchi, A. J., and McClain, C. R.: Biogeochemical modelling of the tropical Pacific Ocean I. Seasonal and interannual variability, *Deep-Sea Res.*, 49, 545–565, 2002. 4330
- 25 Church, J. A. and White, N. J.: A 20th century acceleration in global sea-level rise, *Geophys. Res. Lett.*, 33, L01602, doi:10.1029/2005GL024826, 2006. 4327
- Clementson, L. A., Parslow, J. S., Griffiths, F. B., Lyne, V. D., Mackey, D. J., Harris, G. P., McKenzie, D. C., Bonham, P. I., Rathbone, C. A., and Rintoul, S.: Controls on phytoplankton production in the Australasian sector of the subtropical convergence, *Deep Sea Res.*, 45, 1627–1661, doi:10.1016/S0967-0637(98)00035-1, 1998. 4316
- 30

Evaluation of a near-global eddy-resolving ocean model

P. R. Oke et al.

[Title Page](#)

[Abstract](#)

[Introduction](#)

[Conclusions](#)

[References](#)

[Tables](#)

[Figures](#)

[⏪](#)

[⏩](#)

[◀](#)

[▶](#)

[Back](#)

[Close](#)

[Full Screen / Esc](#)

[Printer-friendly Version](#)

[Interactive Discussion](#)



- Cunningham, S. A., Alderson, S. G., King, B. A., and Brandon, M. A.: Transport and Variability of the Antarctic Circumpolar Current in Drake Passage, *J. Geophys. Res.*, 108, 8084, doi:10.1029/2001JC001147, 2003. 4313, 4340
- Cunningham, S. A., Kanzow, T., Rayner, D., Baringer, M. O., Johns, W. E., Marotzke, J., Longworth, H. R., Grant, E. M., Hirschi, J. J.-M., Beal, L. M., Meinen, C. S., and Bryden, H. L.: Temporal variability of the Atlantic Meridional Overturning Circulation at 26.5° N, *Science*, 317, 935–938, 2007. 4313
- Dai, A. and Trenberth, K. E.: Estimates of freshwater discharge from continents: Latitudinal and seasonal variations, *J. Hydrometeorol.*, 3, 660–687, 2002. 4325
- Dai, A., Qian, T., Trenberth, K. E., and Milliman, J. D.: Changes in continental freshwater discharge from 1948–2004, *J. Climate*, 22, 2773–2791, 2009. 4325
- de Boyer Montegut, C., Madec, G., Fischer, A. S., Lazar, A., and Iudicone, D.: Mixed layer depth over the global ocean: an examination of profile data and a profile-based climatology, *J. Geophys. Res.*, 109, doi:10.1029/2004JC002378, 2004. 4310, 4343
- de Ruijter, W. P. M., Ridderinkhof, H., Lutjeharms, J. R. E., Schouten, M. W., and Veth, C.: Observations of the flow in the Mozambique Channel, *Geophys. Res. Lett.*, 29, 140.1–140.3, 2002. 4317
- Dee, D. P. and Uppala, S.: Variational bias correction of satellite radiance data in the ERA-Interim reanalysis, *Q. J. Roy. Meteorol. Soc.*, 135, 1830–1841, doi:10.1002/qj.493, 2009. 4308, 4325, 4327
- Dencausse, G. and Arhan, M.: Routes of Agulhas rings in the southeastern Cape Basin, *Deep-Sea Res.*, 57, 1406–1421, doi:10.1016/j.dsr.2010.07.008, 2010. 4317
- Dietze, H., Matear, R., and Moore, T.: Nutrient supply to anticyclonic meso-scale eddies off Western Australia estimated with artificial tracers released in a circulation model, *Deep Sea Res.*, 56, 1440–1448, 2009. 4307
- DiMarco, S. F., Chapman, P., Nowlin, W. D., Hacker, P., Donohue, K., Luther, M., Johnson, G. C., and Toole, J.: Volume transport and property distributions of the Mozambique Channel, *Deep Sea Res.*, 49, 1481–1511, 2002. 4315, 4340
- Doos, K., Nycander, J., and Coward, A. C.: Lagrangian decomposition of the Deacon Cell, *J. Geophys. Res.*, 113, C07028, doi:10.1029/2007JC004351, 2008. 4313
- Ducet, N., Traon, P.-Y. L., and Reverdin, G.: Global high-resolution mapping of ocean circulation from TOPEX/POSEIDON and ERS-1 and-2, *J. Geophys. Res.*, 105, 19477–19498, 2000. 4315

- Earth System Research Laboratory: Cooperative Atmospheric Data 951, in: Integration Project: Carbon Dioxide, pp. [CD-ROM], NOAA, Boulder, 952 Colorado, USA, 2009. 4332
- Egbert, G. D., Bennett, A., and Foreman, M.: TOPEX/POSEIDON tides estimated using a global inverse model, *J. Geophys. Res.*, 99, 24821–24852, 1994. 4327
- 5 Everett, J. D., Baird, M. E., Oke, P. R., and Suthers, I. M.: An avenue of eddies: Quantifying the biophysical properties of mesoscale eddies in the Tasman Sea, *Geophys. Res. Lett.*, 39, doi:10.1029/2012GL053091, 2012. 4322
- Follows, M. J., Dutkiewicz, S., Grant, S., and Chisholm, S. W.: Emergent biogeography of microbial communities in a model ocean, *Science*, 315, 1843–1846, doi:10.1126/science.1138544, 2007. 4319
- 10 Garcia, H. E., Locarnini, R. A., Boyer, T. P., and Antonov, J. I.: World Ocean Atlas 2005, Volume 3: Dissolved Oxygen, Apparent Oxygen Utilization, and Oxygen Saturation, in: NOAA Atlas NESDIS 63, edited by Levitus, S., p. 342, U.S. Government Printing Office, Washington, D.C., 2006a. 4331
- 15 Garcia, H. E., Locarnini, R. A., Boyer, T. P., and Antonov, J. I.: World Ocean Atlas 2005, Volume 4: Nutrients (phosphate, nitrate, silicate), in: NOAA Atlas NESDIS 64, edited by Levitus, S., p. 396, U.S. Government Printing Office, Washington, D.C., 2006b. 4331
- Gordon, A. L., Sprintall, J., Van Aken, H. M., Susanto, D., Wijffels, S. E., Molcard, R., Ffield, A., Pranowo, W., and Wirasantosa, S.: The Indonesian throughflow during 2004–2006 as observed by the INSTANT program, *Dynam. Atmos. Oceans*, 50, 115–128, doi:10.1016/j.dynatmoce.2009.12.002, 2010. 4313, 4340, 4348
- 20 Gould, W. J.: Physical Oceanography of the Azores Front, *Progr. Oceanogr.*, 14, 167–190, 1985. 4317
- Griffies, S. M.: *Fundamentals of Ocean Climate Models*, University Press, Princeton, USA, 2004. 4326
- 25 Griffies, S. M.: Elements of MOM4p1, GFDL Ocean Group Technical Report 6, Tech. rep., NOAA/Geophysical Fluid Dynamics Laboratory, 2009. 4308, 4324
- Griffies, S. M. and Hallberg, R. W.: Biharmonic friction with a Smagorinsky-like viscosity for use in large-scale eddy-permitting ocean models, *Mon. Wea. Rev.*, 128, 2935–2946, 2000. 4327
- 30 Hamilton, P., Larsen, J. C., Leaman, K. D., Lee, T. N., and Waddell, E.: Transports through the Straits of Florida, *J. Phys. Oceanogr.*, 35, 308–322, 2004. 4315
- Hundsdorfer, W. and Trompert, R. A.: Method of lines and direct discretization: a comparison for linear advection, *Appl. Numer. Mathematics*, 13, 469–490, 1994. 4326

Evaluation of a near-global eddy-resolving ocean model

P. R. Oke et al.

[Title Page](#)[Abstract](#)[Introduction](#)[Conclusions](#)[References](#)[Tables](#)[Figures](#)[Back](#)[Close](#)[Full Screen / Esc](#)[Printer-friendly Version](#)[Interactive Discussion](#)

Evaluation of a near-global eddy-resolving ocean model

P. R. Oke et al.

[Title Page](#)

[Abstract](#)

[Introduction](#)

[Conclusions](#)

[References](#)

[Tables](#)

[Figures](#)



[Back](#)

[Close](#)

[Full Screen / Esc](#)

[Printer-friendly Version](#)

[Interactive Discussion](#)

- Kawabe, M.: Variations of current path, velocity, and volume transport of the Kuroshio in relation with the large meander, *J. Phys. Oceanogr.*, 25, 3103–3117, 1995. 4317
- Key, R., Kozyr, A., Sabine, C. L., Lee, K., Wanninkhof, R., Bullister, J. L., Feely, R. A., Millero, F. J., Mordy, C., and Peng, T. H.: A global ocean carbon climatology: Results from Global Data Analysis Project (GLODAP), *Global Biogeochem. Cy.*, 18, GB4031, doi:10.1029/2004GB002247, 2004. 4331, 4332
- Kidston, M., Matear, R. J., and Baird, M. E.: Parameter optimisation of a marine ecosystem model at two contrasting stations in the Sub-Antarctic Zone, *Deep Sea Res.*, 58, 2301–2315, 2011. 4308
- Kohl, A. and Stammer, D.: Interannual to decadal changes in the ECCO Global Synthesis, *J. Phys. Oceanogr.*, 37, 313–337, 2007. 4313
- Langlais, C., Schiller, A., and Oke, P. R.: Southern Ocean Fronts in the Bluelink Reanalysis, *Mercator Quarterly Newsletter*, 36, 50–57, 2010. 4307
- Lee, H.-C., Rosati, A., and Spelman, M.: Barotropic tidal mixing effects in a coupled climate model: ocean conditions in the northern Atlantic, *Ocean Modell.*, 11, 464–470, 2006. 4326
- Lenton, A. and Matear, R. J.: Role of the Southern Annular Mode (SAM) in Southern Ocean CO₂ uptake, *Global Biogeochem. Cy.*, 21, GB2016, doi:10.1029/2006GB002714, 2007. 4331
- Lenton, A., Metzl, N., Takahashi, T., Kuchinke, M., Matear, R. J., Roy, T., Sutherland, S. C., Sweeney, C., and Tilbrook, B.: The observed evolution of oceanic pCO₂ and its drivers over the last two decades, *Global Biogeochem. Cy.*, 26, 14 pp., GB2021, doi:10.1029/2011GB004095, 2012. 4331
- Locarnini, R. A., Mishonov, A. V., Antonov, J. I., Boyer, T. P., and Garcia, H. E.: World Ocean Atlas 2005, Volume 1: Temperature, in: NOAA Atlas NESDIS 61, edited by Levitus, S., p. 182, U.S. Government Printing Office, Washington, D.C., 2006. 4331
- Maltrud, M. E. and McClean, J. L.: An eddy resolving global 1/10° ocean simulation, *Ocean Modell.*, 8, 31–54, 2005. 4313, 4317
- Masumoto, Y. and Meyers, G.: Forced Rossby waves in the southern tropical Indian Ocean, *J. Geophys. Res.*, 103, 27589–27602, 1998. 4320
- Matear, R. J.: Parameter optimization and analysis of ecosystem models using simulated annealing: A case study at Station P, *J. Mar. Res.*, 53, 571–607, 1995. 4309

Evaluation of a near-global eddy-resolving ocean model

P. R. Oke et al.

[Title Page](#)

[Abstract](#)

[Introduction](#)

[Conclusions](#)

[References](#)

[Tables](#)

[Figures](#)

[⏪](#)

[⏩](#)

[◀](#)

[▶](#)

[Back](#)

[Close](#)

[Full Screen / Esc](#)

[Printer-friendly Version](#)

[Interactive Discussion](#)



- Matear, R. J. and Hirst, A. C.: Long term changes in dissolved oxygen concentrations in the ocean caused by protracted global warming, *Global Biogeochem. Cy.*, 17, 1125–1144, 2003. 4309
- Matear, R. J. and Lenton, A.: Impact of Historical Climate Change on the Southern Ocean Carbon Cycle, *J. Climate*, 21, 5820–5834, 2008. 4309
- Mongin, M., Matear, R. J., and Chamberlain, M.: Simulation of chlorophyll and iron supplies in the Sub-Antarctic Zone South of Australia, *Deep Sea Res.*, 58, 2126–2134, 2011. 4309, 4330
- Mongin, M. M., Abraham, E. R., and Trull, T. W.: Winter advection of iron can explain the summer phytoplankton bloom that extends 1000 km downstream of the Kerguelen Plateau in the Southern Ocean, *J. Mar. Res.*, 67, 225–237, 2009. 4330
- Moore, T. M., Matear, R. J., Marra, J., and Clementson, L.: Phytoplankton variability off the Western Australian Coast: Mesoscale eddies and their role in cross-shelf exchange, *Deep Sea Res.*, 54, 943–960, 2007. 4316
- Moore, T. S., Campbell, J. W., and Dowell, M. D.: A class-based approach to characterizing and mapping the uncertainty of the MODIS ocean chlorophyll product, *Remote Sens. Environ.*, 113, 2424 – 2430, doi:10.1016/j.rse.2009.07.016, 2009. 4316
- O’Carroll, A. G., Eyre, J. R., and Saunders, R. W.: Three-Way Error Analysis between AATSR, AMSR-E, and In Situ Sea Surface Temperature Observations, *J. Atmos. Ocean. Technol.*, 25, 1197–1207, 2008. 4318
- Oke, P. R. and Griffin, D. A.: The cold-core eddy and strong upwelling off the coast of New South Wales in early 2007, *Deep Sea Res.*, 58, 574–591, doi:10.1016/j.dsr2.2010.06.006, 2011. 4307
- Oke, P. R. and Schiller, A.: Impact of Argo, SST, and altimeter data on an eddy-resolving ocean reanalysis, *Geophys. Res. Lett.*, 34, L19601, doi:10.1029/2007GL031549, 2007. 4307
- Oke, P. R., Schiller, A., Griffin, D. A., and Brassington, G. B.: Ensemble data assimilation for an eddy-resolving ocean model of the Australian region, *Q. J. Roy. Meteorol. Soc.*, 131, 3301–3311, doi:10.1256/qj.05.95, 2005. 4307, 4323
- Oke, P. R., Brassington, G. B., Griffin, D. A., and Schiller, A.: The Bluelink Ocean Data Assimilation System (BODAS), *Ocean Modell.*, 21, 46–70, doi:10.1016/j.ocemod.2007.11.002, 2008. 4307, 4323
- Qiu, B. and Miao, W.: Kuroshio Path Variations South of Japan: Bimodality as a Self-Sustained Internal Oscillation, *J. Phys. Oceanogr.*, 30, 2124–2137, 2000. 4317

Evaluation of a near-global eddy-resolving ocean model

P. R. Oke et al.

[Title Page](#)

[Abstract](#)

[Introduction](#)

[Conclusions](#)

[References](#)

[Tables](#)

[Figures](#)

[⏪](#)

[⏩](#)

[◀](#)

[▶](#)

[Back](#)

[Close](#)

[Full Screen / Esc](#)

[Printer-friendly Version](#)

[Interactive Discussion](#)



- Reynolds, R. W., Smith, T. M., Liu, C., Chelton, D. B., Casey, K. S., and Schlax, M. G.: Daily high-resolution-blended analyses for sea surface temperature, *J. Climate*, 20, 5473–5496, doi:10.1175/2007JCLI1824.1, 2007. 4311, 4313, 4325
- Ridgway, K. R. and Dunn, J. R.: Mesoscale structure of the mean East Australian Current System and its relationship with topography, *Progr. Oceanogr.*, 56, 189–222, doi:10.1016/S0079-6611(03)00004-1, 2003. 4310, 4325, 4326, 4343
- Rintoul, S. R. and Sokolov, S.: Baroclinic transport variability of the Antarctic Circumpolar Current south of Australia (WOCE repeat section SR3), *J. Geophys. Res.*, 106, 2795–2814, 2001. 4313, 4340
- Rio, M.-H., Schaeffer, P., Moreaux, G., Lemoine, J.-M., and Bronner, E.: A new Mean Dynamic Topography computed over the global ocean from GRACE data, altimetry and in-situ measurements, *OceanObs09*, 21–25 September 2009, Venice, 2009. 4309
- Sarmiento, J. and Gruber, N.: *Ocean biogeochemical dynamics*, Princeton University Press, N. J., 2006. 4332
- Schartau, M. and Oschlies, A.: Simultaneous data-based optimization of a 1D-ecosystem model at three locations in the North Atlantic: Part I – Method and parameter estimates, *J. Mar. Res.*, 61, 765–793, 2003. 4341
- Schiller, A., Oke, P. R., Brassington, G. B., Entel, M., Fiedler, R., Griffin, D. A., and Mansbridge, J. V.: Eddy-resolving ocean circulation in the Asian-Australian region inferred from an ocean reanalysis effort, *Progr. Oceanogr.*, 76, 334–365, doi:10.1016/j.pocean.2008.01.003, 2008. 4307, 4323
- Schiller, A., Ridgway, K. R., Steinberg, C. R., and Oke, P. R.: Dynamics of three anomalous SST events in the Coral Sea, *Geophys. Res. Lett.*, 36, L06606, doi:10.1029/2008GL036997, 2009. 4307
- Schiller, A., Wijffels, S. E., Sprintall, J., Molcard, R., and Oke, P. R.: Pathways of intraseasonal variability in the Indonesian Throughflow region, *Dynam. Atmos. Oceans*, 50, 174–200, doi:10.1016/j.dynatmoce.2010.02.003, 2010. 4307
- Smith, N. R.: The Global Ocean Data Assimilation Experiment, *Adv. Space Res.*, 25, 1089–1098, 2000. 4306
- Sun, C., Feng, M., Matear, R., Chamberlain, M., Craig, P., Ridgway, K., and Schiller, A.: Marine downscaling of a future climate scenario for Australian boundary currents, *J. Climate*, 25, 2947–2962, doi:10.1175/JCLI-D-11-00159.1, 2012. 4307

Evaluation of a near-global eddy-resolving ocean model

P. R. Oke et al.

[Title Page](#)

[Abstract](#)

[Introduction](#)

[Conclusions](#)

[References](#)

[Tables](#)

[Figures](#)

[⏪](#)

[⏩](#)

[◀](#)

[▶](#)

[Back](#)

[Close](#)

[Full Screen / Esc](#)

[Printer-friendly Version](#)

[Interactive Discussion](#)

Sweby: High-resolution schemes using flux limiters for hyperbolic conservation laws, *IAM Journal of Numerical Analysis*, 21, 995–1011, 1984. 4326

Takahashi, T., Sutherland, S. C., Wanninkhof, R., Sweeney, C., Feely, R. A., Chipman, D. W., Hales, B., Friederich, G., Chavez, F., Sabine, C., Watson, A., Bakker, D. C., Schuster, U., Metzl, N., Yoshikawa-Inoue, H., Ishii, M., Midorikawa, T., Nojiri, Y., Körtzinger, A., Steinhoff, T., Hoppema, M., Olafsson, J., Arnarson, T. S., Tilbrook, B., Johannessen, T., Olsen, A., Bellerby, R., Wong, C., Delille, B., Bates, N., and de Baar, H. J.: Climatological mean and decadal change in surface ocean pCO₂, and net sea-air CO₂ flux over the global oceans, *Deep Sea Res. Pt. II: Topical Studies in Oceanography*, 56, 554–577, doi:10.1016/j.dsr2.2008.12.009, 2009. 4331

Taylor, A. H., Geider, R. J., and Gilbert, F. J. H.: Seasonal and latitudinal dependencies of phytoplankton carbon- to-chlorophyll a ratios: Results of a modelling study, *Mar. Ecol.-Prog. Ser.*, 152, 51–66, 1997. 4316

van Sebille, E., Johns, W. E., and Beal, L.: Does the vorticity flux from Agulhas rings control the zonal pathway of NADW across the South Atlantic?, 117, C05037, 12 pp., doi:10.1029/2011JC007684, 2012. 4318

Wanninkhof, R.: Relationship between wind speed and gas exchange over the ocean, *J. Geophys. Res.*, 97, 7373–7382, 1992. 4309

Waseda, T., Mitsudera, H., Taguchi, B., and Yoshikawa, Y.: On the eddy-Kuroshio interaction: Meander formation process, *J. Geophys. Res.*, 108, 3220, doi:10.1029/2002JC001583, 2003. 4317

Westwood, K., Griffiths, B. F., Webb, J., and Wright, S. W.: Primary production in the Sub-Antarctic and Polar Frontal Zones south of Tasmania, Australia; SAZ-Sense survey, 2007, *Deep Sea Res.*, 58, 21–22, 2011. 4329

Whiteway, T. G.: Australian Bathymetry and Topography Grid, *Geoscience Australia Record*, 21, 46 pp., 2009. 4324

Yamanaka, Y. and Tajika, E.: The role of vertical fluxes of particulate organic material and calcite in the oceanic carbon cycle: Studies using a ocean biogeochemical general circulation model, *Global Biogeochem. Cy.*, 10, 361–382, 1996. 4330

Evaluation of a near-global eddy-resolving ocean model

P. R. Oke et al.

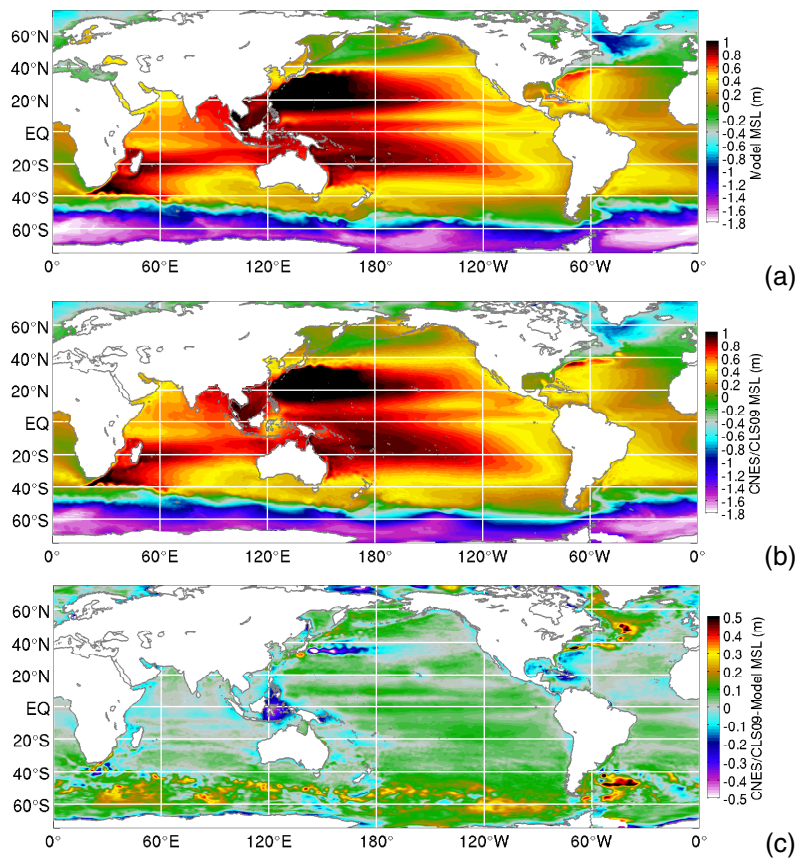


Fig. 1. Comparison of the (a) mean sea-level from the model, (b) the mean dynamic topography from CNES-CLS09 V1.1, and (c) the difference between the CNES-CLS09 and the model MSL field.

Title Page

Abstract Introduction

Conclusions References

Tables Figures

⏪ ⏩

◀ ▶

Back Close

Full Screen / Esc

Printer-friendly Version

Interactive Discussion



Evaluation of a near-global eddy-resolving ocean model

P. R. Oke et al.

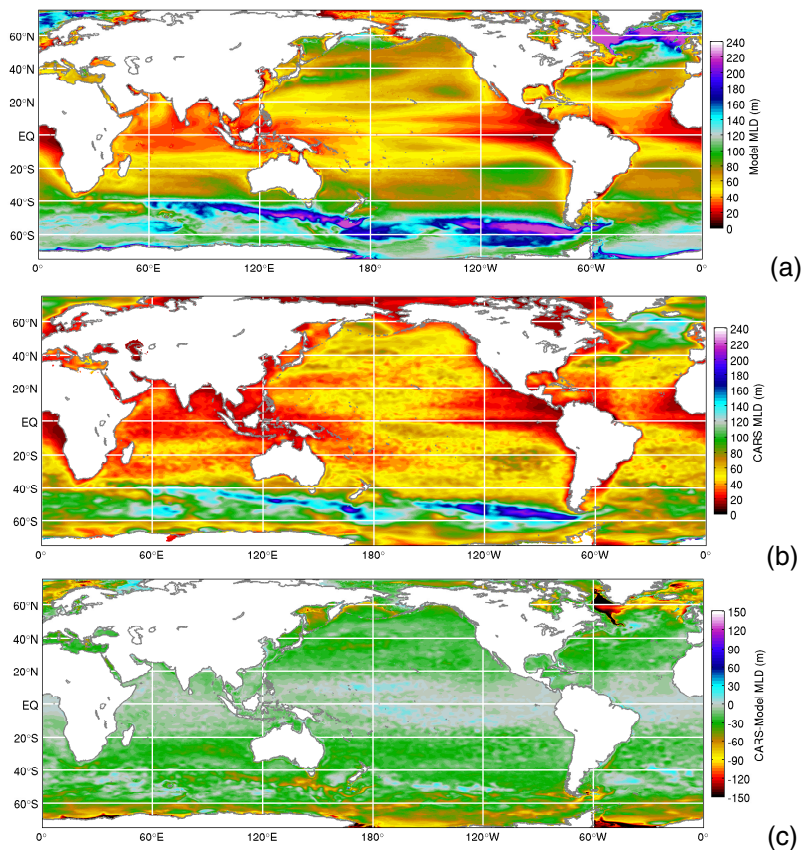


Fig. 2. Comparison of the time-averaged MLD (m) from the **(a)** model, **(b)** CARS (Ridgway and Dunn, 2003), and **(c)** the difference between the CARS and model MLD field. The model MLD is calculated from daily means using the MLD definition described by de Boyer Montegut et al. (2004).

[Title Page](#)[Abstract](#)[Introduction](#)[Conclusions](#)[References](#)[Tables](#)[Figures](#)[⏪](#)[⏩](#)[◀](#)[▶](#)[Back](#)[Close](#)[Full Screen / Esc](#)[Printer-friendly Version](#)[Interactive Discussion](#)

Evaluation of a near-global eddy-resolving ocean model

P. R. Oke et al.

[Title Page](#)

[Abstract](#)

[Introduction](#)

[Conclusions](#)

[References](#)

[Tables](#)

[Figures](#)



[Back](#)

[Close](#)

[Full Screen / Esc](#)

[Printer-friendly Version](#)

[Interactive Discussion](#)

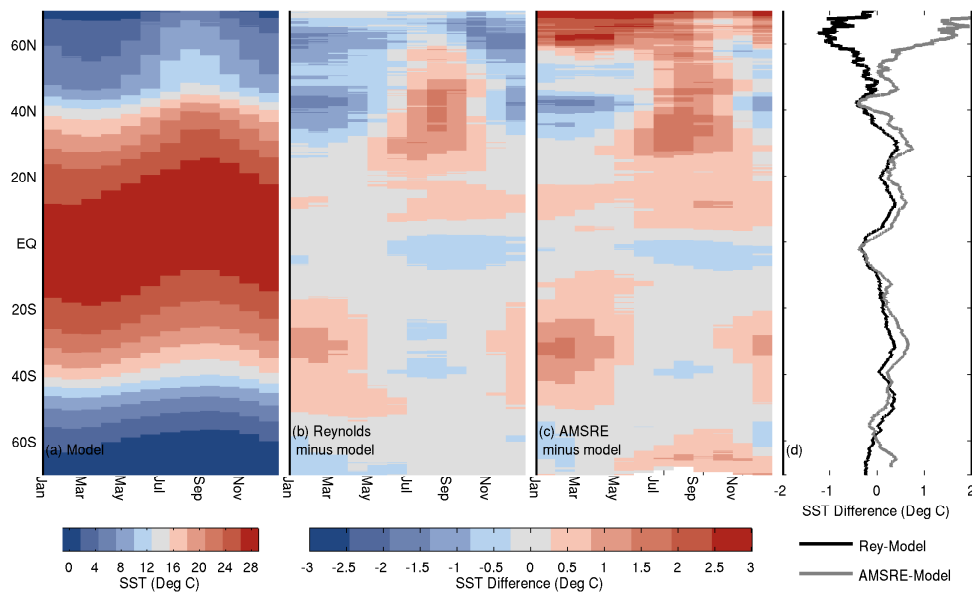


Fig. 3. (a) Seasonal climatology of zonal-average modelled SST, the zonal average of the difference between modelled and observed SST seasonal climatology using (b) Reynolds SST and (c) AMSR-E SST, and (d) the time-averaged and zonally averaged difference between observed and modelled SST.

Evaluation of a near-global eddy-resolving ocean model

P. R. Oke et al.

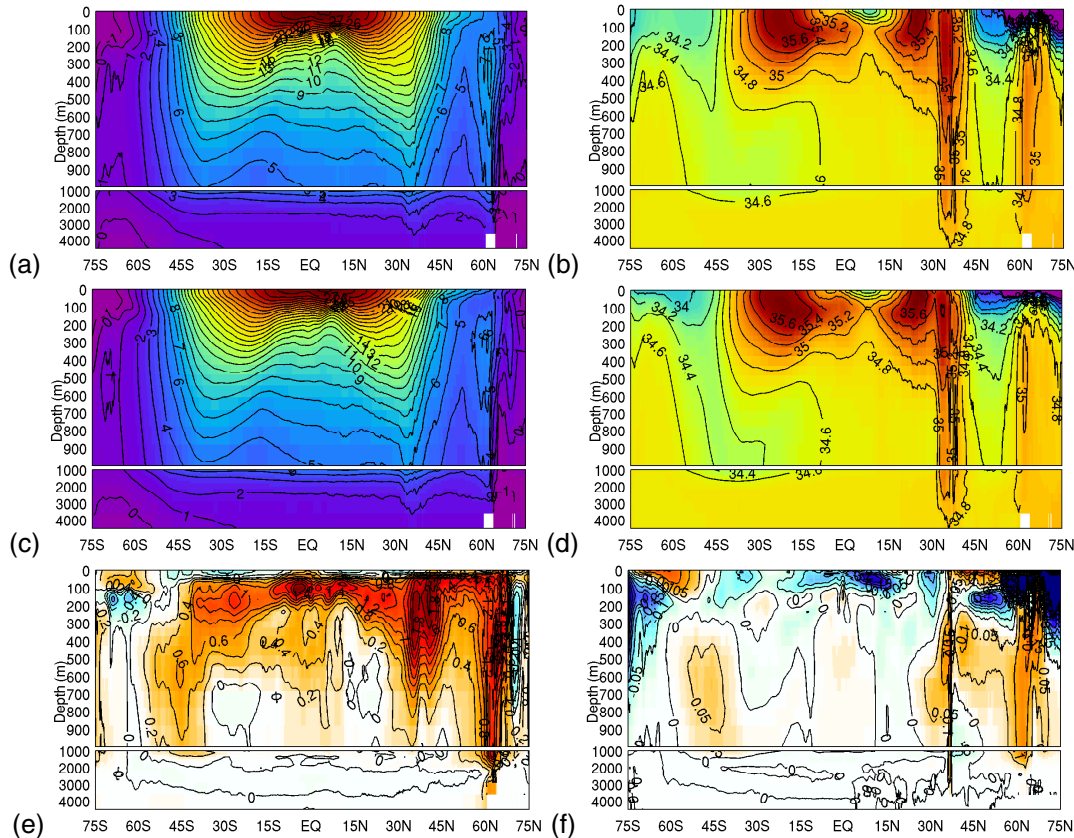


Fig. 4. (a, b) Modelled, (c, d) observed, and (e, f) modelled minus observed time- and zonal-mean temperature (a, c, e) and (b, d, f) salinity. The contour intervals for temperature are 1 °C in panel (a) and 0.2 °C in panel (b). The contour interval for salinity is 0.2 psi in panel (c) and 0.05 psu in panel (d).

[Title Page](#)
[Abstract](#)
[Introduction](#)
[Conclusions](#)
[References](#)
[Tables](#)
[Figures](#)
[⏪](#)
[⏩](#)
[◀](#)
[▶](#)
[Back](#)
[Close](#)
[Full Screen / Esc](#)
[Printer-friendly Version](#)
[Interactive Discussion](#)

Evaluation of a near-global eddy-resolving ocean model

P. R. Oke et al.

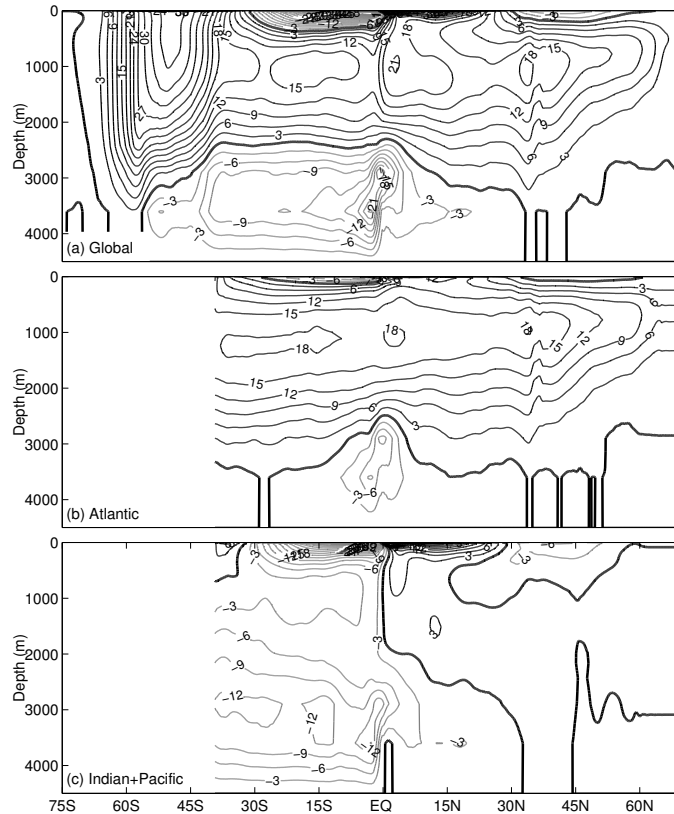


Fig. 5. Time-mean, zonal-averaged meridional overturning streamfunction (S_v) for the **(a)** entire globe, **(b)** Atlantic basin, and **(c)** Indian+Pacific basins. Solid contours are positive (clock-wise), grey contours are negative (anti-clockwise), and bold contours are zero. For clarity, fields have been averaged to eliminate features that are shorter than 1 degree.

[Title Page](#)
[Abstract](#)
[Introduction](#)
[Conclusions](#)
[References](#)
[Tables](#)
[Figures](#)
[⏪](#)
[⏩](#)
[◀](#)
[▶](#)
[Back](#)
[Close](#)
[Full Screen / Esc](#)
[Printer-friendly Version](#)
[Interactive Discussion](#)

**Evaluation of a
near-global
eddy-resolving ocean
model**

P. R. Oke et al.

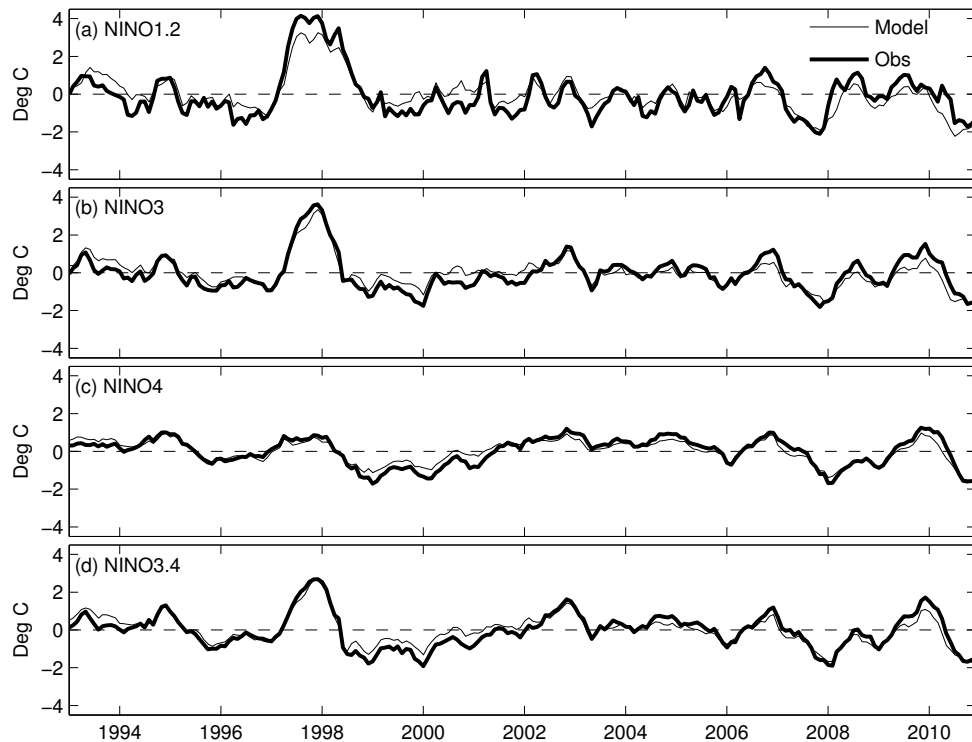
[Title Page](#)[Abstract](#)[Introduction](#)[Conclusions](#)[References](#)[Tables](#)[Figures](#)[Back](#)[Close](#)[Full Screen / Esc](#)[Printer-friendly Version](#)[Interactive Discussion](#)

Fig. 6. Time-series of the (a) NINO1.2, (b) NINO3, (c) NINO4, and (d) NINO3.4 SST anomalies from observations (OSTIAv2) and the model (OFAM3).

Evaluation of a near-global eddy-resolving ocean model

P. R. Oke et al.

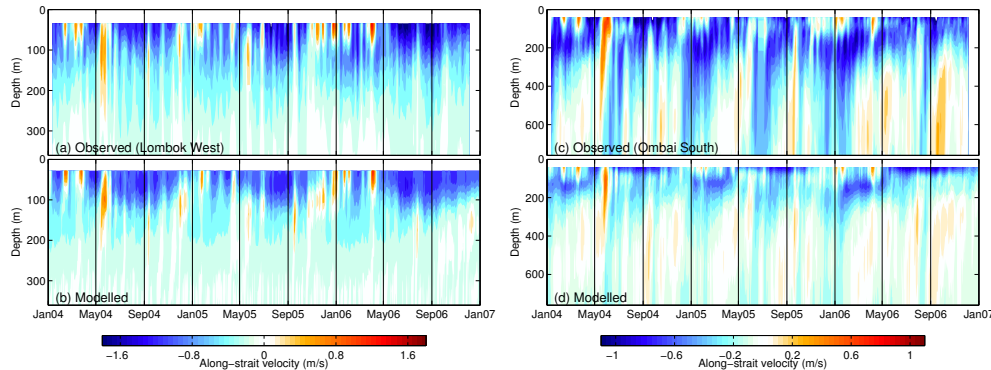


Fig. 7. Time-series of **(a, c)** observed and **(b, d)** modelled along-strait velocity at Lombok **(a–b;** $115^{\circ}45.55' \text{ W}$, $8^{\circ}26.34' \text{ S}$) and Ombai **(c–d;** $125^{\circ}0.384' \text{ E}$, $8^{\circ}38.1' \text{ S}$) Strait during the INSTANT program (Gordon et al., 2010). Negative (blue) velocities indicate flow towards the Indian Ocean, and positive (red) velocities are towards the Indonesian Seas.

[Title Page](#)
[Abstract](#)
[Introduction](#)
[Conclusions](#)
[References](#)
[Tables](#)
[Figures](#)
[⏪](#)
[⏩](#)
[◀](#)
[▶](#)
[Back](#)
[Close](#)
[Full Screen / Esc](#)
[Printer-friendly Version](#)
[Interactive Discussion](#)

Evaluation of a near-global eddy-resolving ocean model

P. R. Oke et al.

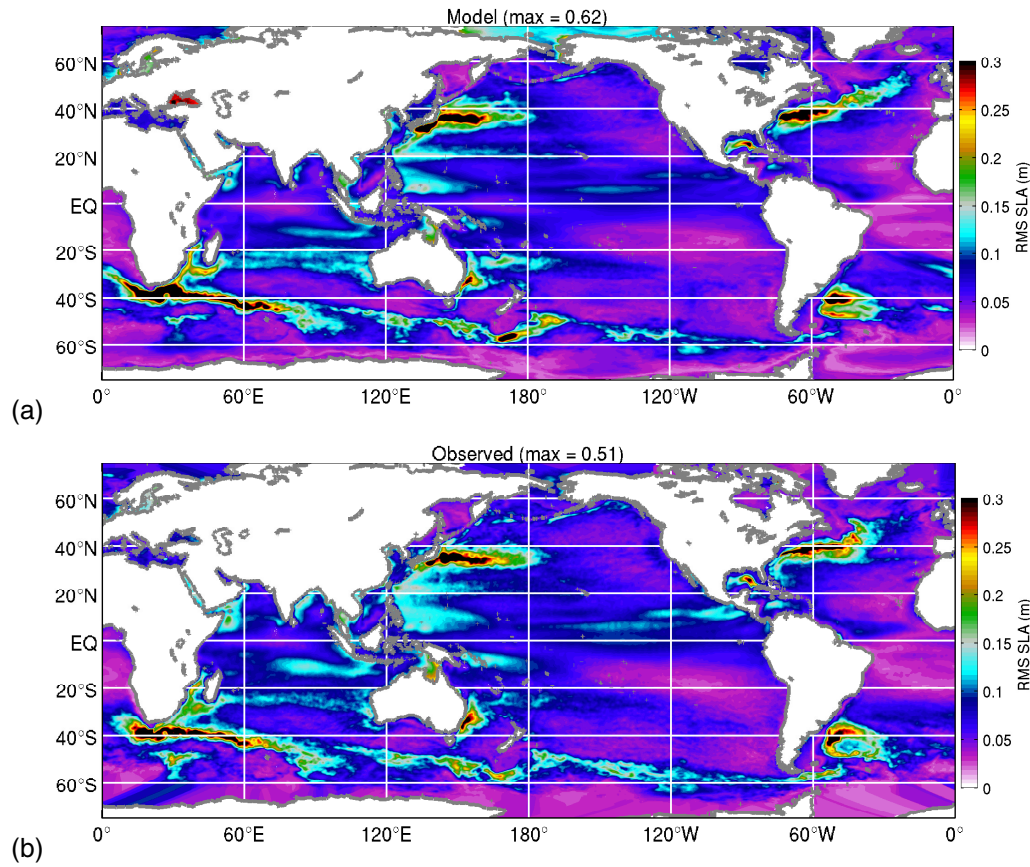


Fig. 8. Comparison of the RMS SLA from the model (top) and observations (bottom). The title of each panel includes the global maximum value of RMS SLA that are off the colour scale used.

[Title Page](#)

[Abstract](#) [Introduction](#)

[Conclusions](#) [References](#)

[Tables](#) [Figures](#)

[⏪](#) [⏩](#)

[◀](#) [▶](#)

[Back](#) [Close](#)

[Full Screen / Esc](#)

[Printer-friendly Version](#)

[Interactive Discussion](#)



Evaluation of a near-global eddy-resolving ocean model

P. R. Oke et al.

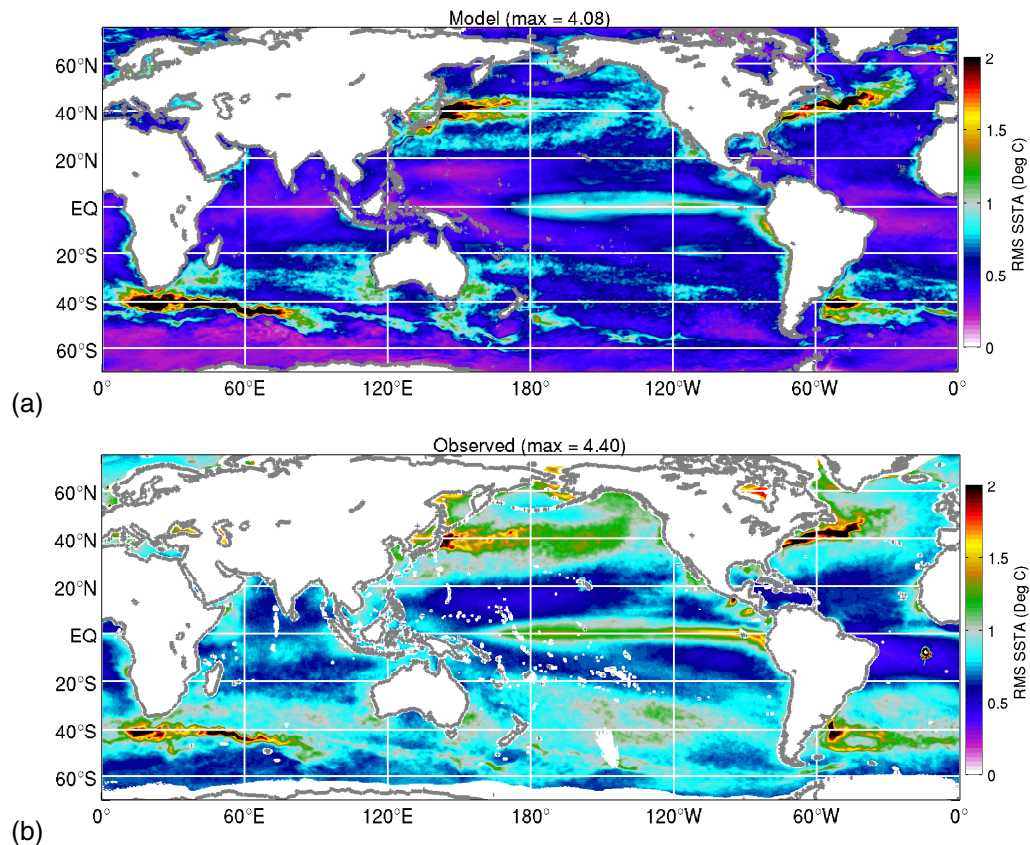


Fig. 9. Comparison of the RMS SSTA from the model (top) and observations (bottom).

[Title Page](#)

[Abstract](#) [Introduction](#)

[Conclusions](#) [References](#)

[Tables](#) [Figures](#)

[⏪](#) [⏩](#)

[◀](#) [▶](#)

[Back](#) [Close](#)

[Full Screen / Esc](#)

[Printer-friendly Version](#)

[Interactive Discussion](#)



**Evaluation of a
near-global
eddy-resolving ocean
model**

P. R. Oke et al.

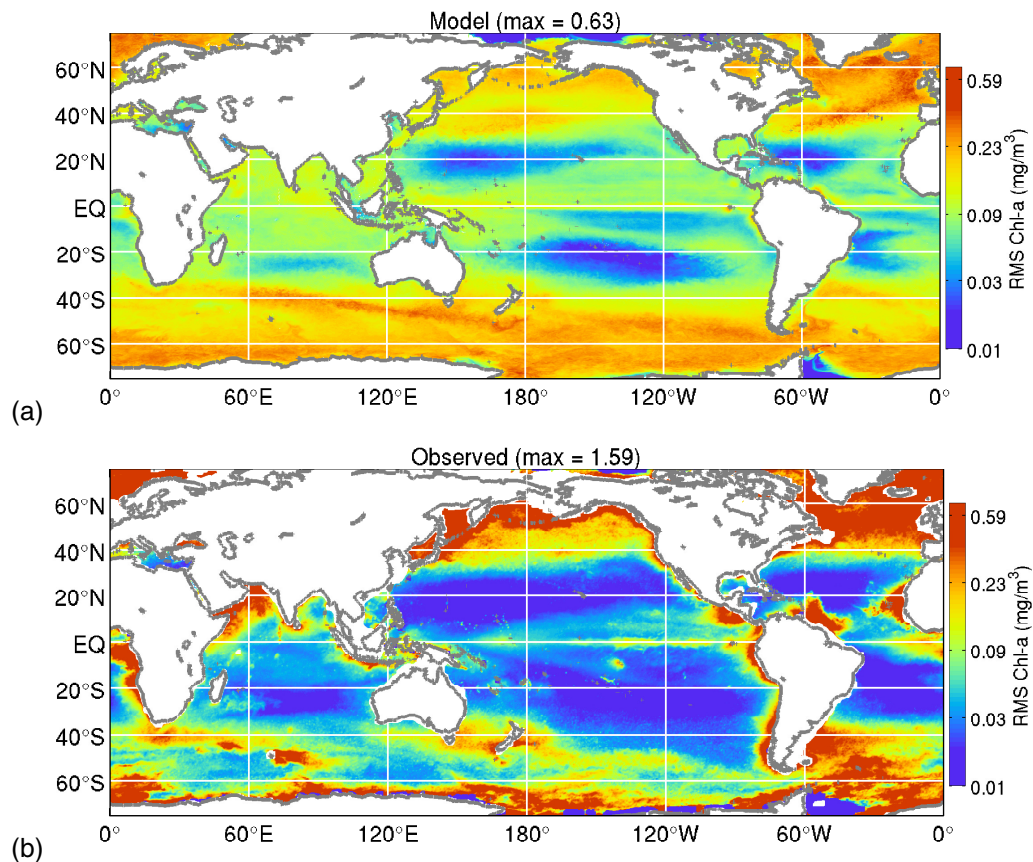


Fig. 10. Comparison of the RMS of the surface Chlorophyll *a* from the model (top) and from SeaWiFS (bottom).

[Title Page](#)[Abstract](#)[Introduction](#)[Conclusions](#)[References](#)[Tables](#)[Figures](#)[⏪](#)[⏩](#)[◀](#)[▶](#)[Back](#)[Close](#)[Full Screen / Esc](#)[Printer-friendly Version](#)[Interactive Discussion](#)

Example of Modelled Surface Phytoplankton

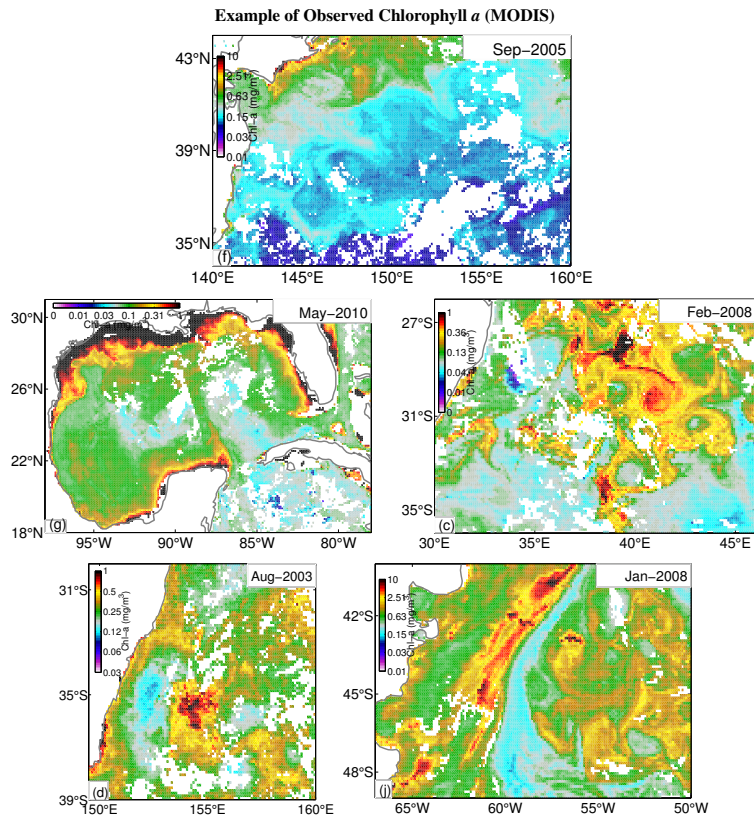


Fig. 11. Example of daily-averaged modelled surface phytoplankton for the (a) Kuroshio, (b) Gulf of Mexico, (c) Agulhas, (d) EAC, and (e) BMC region. The daily-averaged velocity at 50 m depth is overlaid on the model fields, with one vector every 0.4° . The length of each vector represents the trajectory of a particle over 2 days.

Evaluation of a near-global eddy-resolving ocean model

P. R. Oke et al.

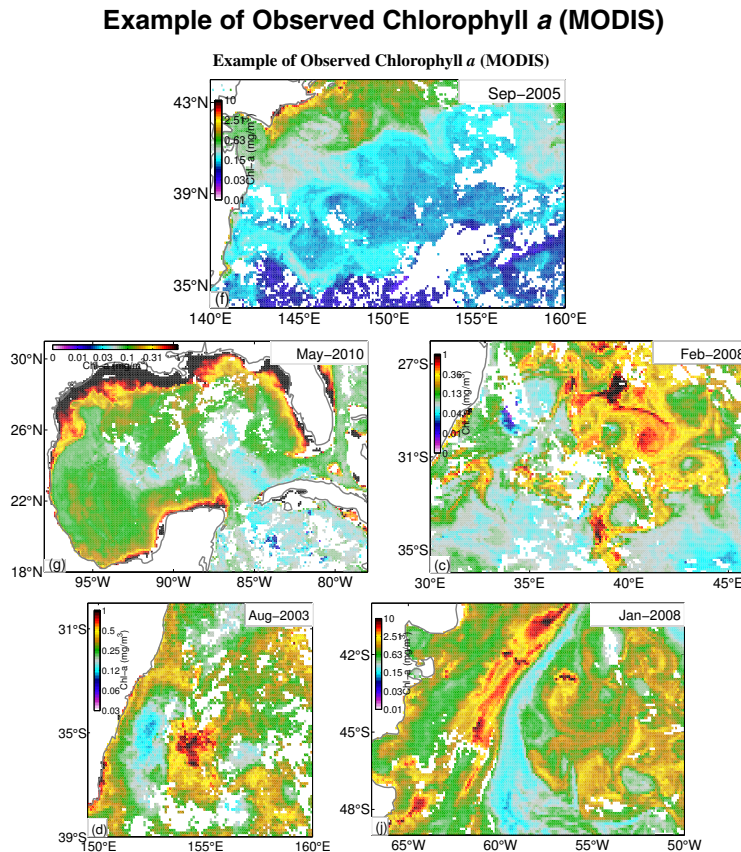


Fig. 12. Example of 8-day composite Chlorophyll *a* from MODIS for the (a) Kuroshio, (b) Gulf of Mexico, (c) Agulhas, (d) EAC, and (e) BMC region.

**Evaluation of a
near-global
eddy-resolving ocean
model**

P. R. Oke et al.

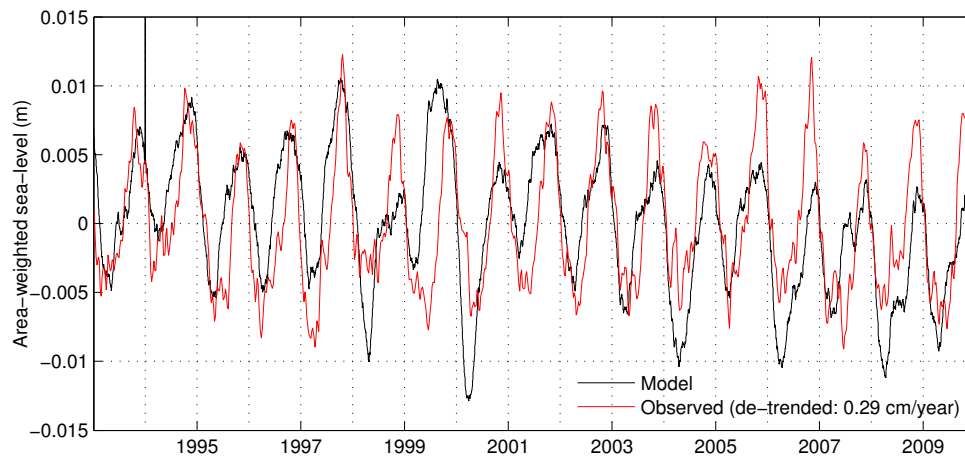


Fig. 13. Time series of area-weighted global-mean sea-level from the model (black) and observations (red), each relative to their own time-means. The linear trend has been removed from the observations that are based on gridded sea-level anomaly maps from Aviso.

[Title Page](#)[Abstract](#)[Introduction](#)[Conclusions](#)[References](#)[Tables](#)[Figures](#)[⏪](#)[⏩](#)[◀](#)[▶](#)[Back](#)[Close](#)[Full Screen / Esc](#)[Printer-friendly Version](#)[Interactive Discussion](#)